The Astrophysical Journal Supplement Series, 267:37 (24pp), 2023 August https://doi.org/10.3847/1538-4365/acda30

A *Quick Look* at the 3 GHz Radio Sky. II. Hunting for DRAGNs in the VLA Sky Survey

Yjan A. Gordon[1], Lawrence Rudnick[2], Heinz Andernach[3,4], Leah K. Morabito[5,6], Christopher P. O'Dea[7], Kaylan-Marie Achong[8,9,12], Stefi A. Baum[7], Caryelis Bayona-Figueroa[9,10,12], Eric J. Hooper[9], Beatriz Mingo[11], Melissa E. Morris[9], and Adrian N. Vantyghem[7]

[1] Department of Physics, University of Wisconsin-Madison, 1150 University Avenue, Madison, WI 53706, USA; yjan.gordon@wisc.edu
[2] Minnesota Institute for Astrophysics, School of Physics and Astronomy, University of Minnesota, 116 Church Street SE, Minneapolis, MN 55455, USA
[3] Thüringer Landessternwarte, Sternwarte 5, D-07778 Tautenburg, Germany
[4] Depto. de Astronomia, Univ. de Guanajuato, Callejón de Jalisco s/n, Guanajuato, C.P. 36023, GTO, Mexico
[5] Centre for Extragalactic Astronomy, Department of Physics, Durham University, South Road, Durham, DH1 3LE, UK
[6] Institute for Computational Cosmology, Department of Physics, Durham University, South Road, Durham DH1 3LE, UK
[7] Department of Physics and Astronomy, University of Manitoba, Winnipeg, MB R3T 2N2, Canada
[8] Department of Physics, University of the West Indies, St. Augustine, Trinidad and Tobago
[9] Department of Astronomy, University of Wisconsin-Madison, 475 N. Charter Street, Madison, WI 53703, USA
[10] Departmento de Ciencias Físicas, Universidad de Puerto Rico, P.O. Box 23323, San Juan, PR 00931-3323, USA
[11] School of Physical Sciences, The Open University, Walton Hall, Milton Keynes, MK7 6AA, UK
Received 2023 March 21; revised 2023 May 19; accepted 2023 May 21; published 2023 August 3

Abstract

Active galactic nuclei (AGNs) can often be identified in radio images as two lobes, sometimes connected to a core by a radio jet. This multicomponent morphology unfortunately creates difficulties for source finders, leading to components that are (a) separate parts of a wider whole, and (b) offset from the multiwavelength cross identification of the host galaxy. In this work we define an algorithm, DRAGNHUNTER, for identifying double radio sources associated with AGNs (DRAGNs) from component catalog data in the first epoch *Quick Look* images of the high-resolution ($\approx 3''$ beam size) Very Large Array Sky Survey (VLASS). We use DRAGNHUNTER to construct a catalog of >17,000 DRAGNs in VLASS for which contamination from spurious sources is estimated at ≈11%. A "high-fidelity" sample consisting of 90% of our catalog is identified for which contamination is <3%. Host galaxies are found for ≈13,000 DRAGNs as well as for an additional 234,000 single-component radio sources. Using these data, we explore the properties of our DRAGNs, finding them to be typically consistent with Fanaroff–Riley class II sources and to allow us to report the discovery of 31 new giant radio galaxies identified using VLASS.

Unified Astronomy Thesaurus concepts: Radio astronomy (1338); Radio galaxies (1343); Giant radio galaxies (654); Extragalactic radio sources (508); Active galactic nuclei (16)

Supporting material: machine-readable tables

1. Introduction

Active galactic nuclei (AGNs), where the accretion of matter onto a galaxy's central supermassive black hole is readily detectable, represent a key phase in a galaxy's evolution (e.g., Ferrarese & Merritt 2000; Croton 2006; Harrison 2017). A few percent of AGNs are able to launch two oppositely directed jets of relativistic plasma that produce powerful radio emission (e.g., Padovani 2017; Blandford et al. 2019; Hardcastle & Croston 2020). These radio-loud AGNs (RLAGNs) have radio properties that likely depend on the black hole mass, spin, and matter accretion rate (e.g., Blandford et al. 2019), as well as the interaction of the radio source with the gaseous environment that it propagates through (e.g., Miley 1980; Heinz et al. 1998; Hubbard & Blackman 2006; Sutherland & Bicknell 2007; Morganti et al. 2021; O'Dea & Saikia 2021).

Early on, Fanaroff & Riley (1974) observed a dichotomy in the morphology of extended radio emission from AGNs, which they used to classify RLAGNs. Class I objects (FR Is) have their radio brightness peaks close to the nucleus, while class II objects (FR IIs) are "edge-brightened" with their brightness peaks being closer to the leading edge of the jet. Subsequent developments in both observations (e.g., Bridle 1984) and theory (e.g., Bicknell 1985) have led to the following paradigm. The jets in lower radio power FR Is interact strongly with their environments and decelerate to nonrelativistic velocities on scales of a few kiloparsecs (e.g., Bicknell 1985; Laing & Bridle 2014). Because the jets in FR Is are nonrelativistic on kiloparsec scales, Doppler boosting effects are minimal, and both jets are observed. The jets expand as they propagate outwards and become diffuse plumes, resulting in the brightness peaks being near the nucleus. On the other hand, in the FR II sources, the jets do not interact as strongly with the environment and remain relativistic all the way out to the terminal shock at the end of the jet (e.g., Garrington et al. 1988; Laing 1988). The Doppler boosting that occurs when the axis is close to the line of sight results in the jet pointing toward the observer being brighter than that in the opposite direction. Conversely, when the jet axis is closer to the plane of the sky, neither jet is significantly Doppler boosted with respect to the observer and often no or faint jets are seen. The terminal shock (or working surface) produces bright radio emission (called a hotspot) and thus the source brightness peaks near the outer

[12] Kaylan-Marie Achong and Caryelis Bayona-Figueroa are summer students at the National Radio Astronomy Observatory.

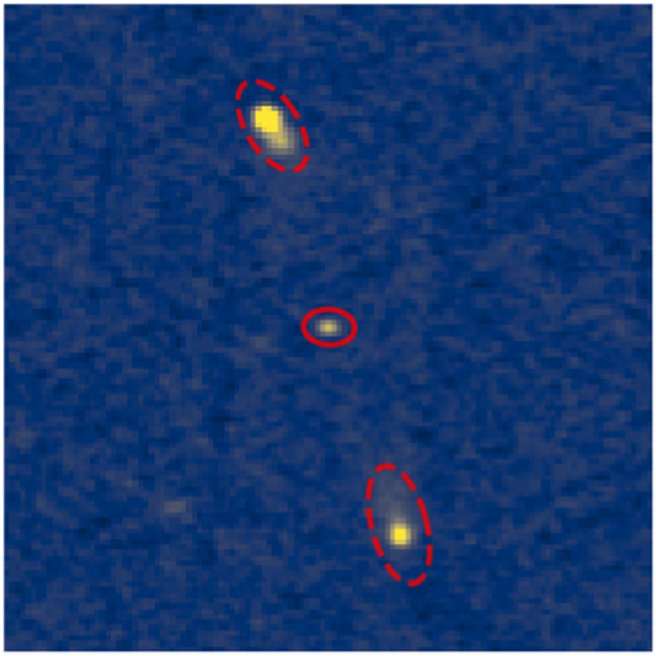

Figure 1. Example of how double and triple radio sources can be split into multiple detections in radio "source" catalogs. The VLASS image of the source is shown by the blue/yellow color map, with the cataloged components marked by red ellipses. The ellipse geometry in this figure is defined by the *fitted* component geometry from the catalog of Gordon et al. (2021) with the major and minor axes multiplied by a factor of 3 to aid visibility in this figure. The ellipses with dashed lines show components that are resolved by VLASS, while the ellipse shown with a solid line is a point source and has a deconvolved size of zero.

edges of the source. At the hotspot, the jet plasma spreads sideways inflating a radio lobe (e.g., Blandford & Rees 1974; Norman et al. 1982; Begelman & Cioffi 1989) producing the "classical double" radio structure. These double-lobed radio galaxies have become known as double radio sources associated with AGNs, or DRAGNs (Leahy 1993; Leahy & Perley 1995).

The current era of blind radio continuum surveys over large swathes of the sky is producing observations of millions of radio galaxies (Condon et al. 1998; Norris et al. 2011; Norris 2017; Gordon et al. 2021; Hale et al. 2021; Shimwell et al. 2022). The majority of RLAGNs in blind surveys will appear as compact sources as a consequence of the limited angular resolution of the surveys and the predominance of intrinsically compact radio sources (O'Dea & Baum 1997; Reynolds & Begelman 1997; Alexander 2000). Nonetheless, given the millions of RLAGNs that will be observed, a large number of DRAGNs can be expected in survey imaging.

Identifying DRAGNs in survey data presents unique challenges. Cataloging "sources" in any astronomical imaging is typically achieved with a "source-finding" algorithm that looks for regions of intensity above a predefined threshold (e.g., 5× the rms noise). In the case of DRAGNs however—and indeed more complex radio morphologies—this approach can lead to the two lobes being identified as separate "sources" even though they belong to the same physical object. We show a textbook example of this complication in Figure 1 using an image from the Karl G. Jansky Very Large Array (VLA) Sky Survey (VLASS; Lacy et al. 2020) and the associated catalog (Gordon et al. 2021). In this particular example, the DRAGN is modeled as three distinct "sources" in the catalog (red ellipses in Figure 1).

Identification of DRAGNs in survey imaging is generally dependent on visual inspection (Banfield et al. 2015; Vardoulaki et al. 2021; Gürkan et al. 2022), or, increasingly, on machine learning (Galvin et al. 2019; Wu et al. 2019; Scaife & Porter 2021). The former approach is well suited to small data sets, but can be impractical for the large data sets of current- and next-generation wide-field surveys. The latter approach is often dependent on large training sets of pre-identified and labeled morphological classifications. Moreover, it is often necessary to specifically tailor machine-learning algorithms to each data set as results of different survey characteristics, e.g., angular resolution, observing frequency, and noise levels. While DRAGNs may fool source finders, their morphology is still relatively simple, and as such one can imagine developing algorithms based on grouping "sources" together to identify DRAGNs. Indeed, a number of such algorithms have been used to identify complex-morphology radio sources using survey catalog data (e.g., Magliocchetti et al. 1998; Best et al. 2005; Sadler et al. 2007; Ching et al. 2017). In this paper we define a new algorithm to detect DRAGNs specifically (as the "simplest" complex morphological type) in the VLASS catalog data with minimal contamination from more complex or unrelated sources. This algorithm, which we are calling DRAGNhunter, is then used to build a catalog of DRAGNs in VLASS. We combine this catalog with multiwavelength data to identify the likely host galaxies of these DRAGNs.

The layout of this paper is as follows. In Section 2 we describe the catalog data we use and the DRAGNhunter algorithm with which we identify DRAGNs. Section 3 describes the reliability and completeness of our catalog of DRAGNs. We identify host galaxies and redshifts for our DRAGNs where possible in Section 4. In Section 5 we use the catalog we have produced to explore the general properties of DRAGNs in VLASS, with a focus on triple sources in Section 6. A summary of this paper and a discussion of future work is presented in Section 7. The data model of the catalog accompanying this article is described in the Appendix. In order to differentiate between catalog entries and physical sources, throughout the rest of this paper we use the nomenclature *'component'* to refer to a single detection from a source finder, and reserve *'source'* to mean the physical object. For example, the *source* shown in Figure 1 is a DRAGN composed of three *components*. Where referring to spectral index, α, we use the convention where spectral index is related to flux density, S, by $S_\nu \propto \nu^\alpha$. A flat ΛCDM cosmology is adopted throughout, with: $h = 0.7$, $H_0 = 100\,h$ km s^{-1} Mpc^{-1}, $\Omega_m = 0.3$, and $\Omega_\Lambda = 0.7$.

2. Identifying DRAGNs from Radio Component Data

2.1. VLASS Catalog Data

VLASS is an ongoing survey to provide multiepoch $\nu \sim 3$ GHz mapping of the entire sky north of $-40°$ in decl. at high resolution (Lacy et al. 2020). The first epoch of VLASS was completed in 2019, and rapidly produced *Quick Look* images covering ≈34,000 deg^2 are publicly available. These *Quick Look* images have a typical rms noise level of 140 μJy beam^{-1} (Gordon et al. 2021). For this work we make use of the catalog of components in the *Quick Look* images of VLASS epoch 1

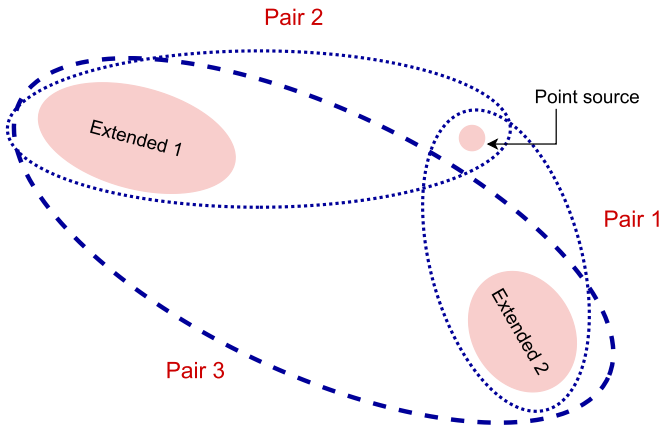

Figure 2. A representation of the approach DRAGNHUNTER takes to looking for radio doubles. Three model radio components are shown in this schematic, two of which are extended, while one is a point source at the resolution of the image. In this scenario the two extended components may represent two lobes of a radio galaxy, and the point source may be an associated core or entirely unrelated. If one were to just search for the nearest neighbor blindly, then the two pairs represented by the dotted blue ellipses (Pair 1 and Pair 2) would be selected. However, by excluding point sources from the pair finding, DRAGNHUNTER will select Pair 3 (blue dashed ellipse) instead.

presented in Gordon et al. (2021). Following the recommendations in Section 3 of Gordon et al. (2021), we only consider components satisfying `S_Code` $\neq$ "E," `Quality_flag`$==$ (0|4) and `Duplicate_flag` < 2. These criteria are designed to limit contamination by spurious detections arising from the limited quality of the VLASS *Quick Look* images, as well potential duplicates resulting from overlaps between images (for a full discussion of these criteria, see Gordon et al. 2021).

The median beam size of VLASS in epoch 1 is $2\farcs9$, the smallest of any near-all-sky radio continuum survey to date. While a number of narrower field surveys use smaller beams, e.g., the VLA-COSMOS surveys (Schinnerer et al. 2004, 2007; Smolčić et al. 2017) and the LOFAR-deep high-definition fields (Sweijen et al. 2022), such very-high-resolution projects only cover of the order a few square degrees of the sky. The combination of high angular resolution and near-all-sky coverage of VLASS makes the survey ideally suited to identifying large numbers of sources in the radio sky and differentiating those that are genuinely compact from sources that have extended radio morphologies.

Unless dominated by hotspot emission, the lobes of DRAGNs are expected to have extended radio morphologies, rather than appear pointlike in high-resolution imaging. The ability of VLASS to cleanly differentiate compact and extended radio morphologies can thus be exploited to find radio detections that are more likely to be a radio lobe than a radio core. Furthermore, extended-morphology radio sources generally have steeper radio spectra than the pointlike sources, likely resulting from the contribution of flat-spectrum radio cores to the unresolved source population (Gordon et al. 2021; Norris et al. 2021); this can be utilized with future releases of VLASS single epoch images (Lacy et al. 2022).

2.2. Finding Pairs of Lobes

The algorithm we use to search for DRAGNs, DRAGNHUNTER, is primarily searching for nearest neighbor pairs of likely radio *lobes*, rather than just any pairing of detected radio *components*. This distinction is important, as searching for just pairs of radio *components* will likely result in some pairings

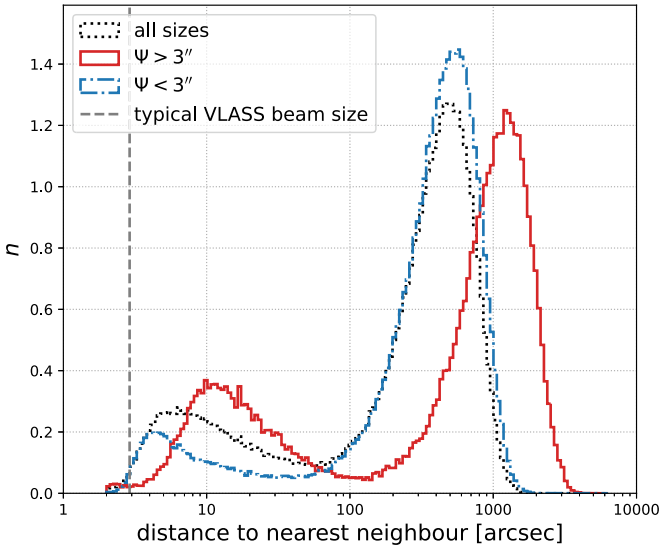

Figure 3. Distribution of angular distance between the nearest neighbor for three different populations of VLASS components with $S_{\rm peak} > 3$ mJy beam^{-1}. The red solid line shows those with a deconvolved angular size, Ψ, $>3''$ (candidate lobes). For comparison, the blue dotted–dashed line shows the distribution for components with $\Psi < 3''$ (not considered as candidate lobes). The black dotted line shows the nearest neighbor distances without applying a size cut, and the gray dashed vertical line represents the typical VLASS beam size.

that do not represent the full radio source (e.g., a pair consisting of a radio core and a radio lobe; see Figure 2) or that are completely unrelated to one another. While it is impossible to select only radio lobes just from radio component catalog data, the component geometry can be used to find those components that are more extended, and thus more likely to represent radio lobe detections.

In Gordon et al. (2021) we showed that reliability of the flux density measurements in the VLASS quick look component catalog lessens at $S_{\rm peak} < 3$ mJy beam^{-1}. Therefore we only include components brighter than 3 mJy beam^{-1} in this work. We wish to identify extended components as candidate lobes. Given the median beam size in VLASS epoch 1 is $2\farcs9$, we consider components with a major axis after deconvolution from the beam, Ψ, greater than $3''$ to be cleanly extended. While the subtraction of the beam from the image would allow us to measure extents well below the beam size, this of course comes with an increase in the relative uncertainty in the measured size —the mean relative error in angular size for components with $\Psi < 3''$ is $\approx$7%, whereas for those with $\Psi > 3''$ the mean relative error is $\approx$4%. Larger components thus represent a conservative selection of candidate lobes where the flux density measurement is considered reliable, and the extent of the component is cleanly resolved. Naturally, relaxing these criteria would allow for the detection of more DRAGNs but likely at lower confidence (see Section 3). A search for pairs of such lobe candidates returns 80,325 unique "nearest neighbor" pairs, i.e., the same pair is not repeated with the component order swapped. In cases where a component is associated with multiple pairs by virtue of being the nearest neighbor of at least one other candidate lobe, we flag the pair with the smallest angular separation as the preferred pair, resulting in a sample of 72,832 pairs of candidate lobes.

In Figure 3 we show the distribution of angular separation to the nearest neighbor for three different selections of components with $S_{\rm peak} > 3$ mJy beam^{-1}. The black dotted line shows

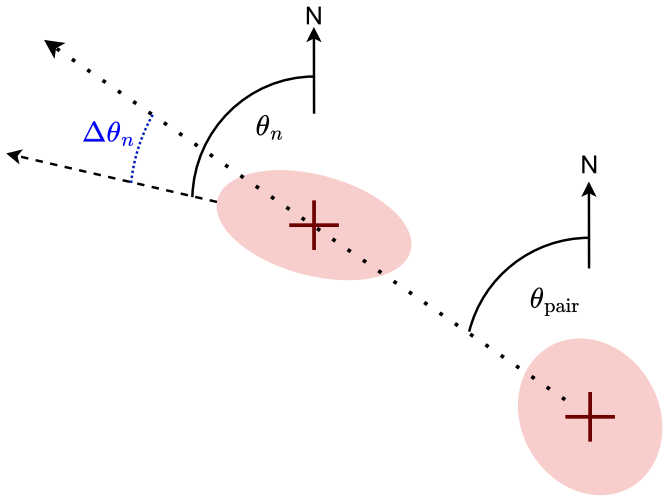

Figure 4. Schematic showing how component (mis)alignment is determined by DRAGNhunter. For any pair of components, the position angle of the axis of the pair, $\theta_{\rm pair}$, provides a reference by which to measure the alignment of the two components (pink ellipses, red crosses mark the central position of the components). Each component has its own position angle, θ_n, which can be compared to $\theta_{\rm pair}$ giving an alignment of component n relative to the pair axis, $\Delta\theta_n$ (shown in blue) with a value between 0° and 90°. For clarity θ_n and $\Delta\theta_n$ are only shown for the component on the left-hand side in this figure, but measurements for both components are determined.

components of all sizes, the blue dashed–dotted line shows components with $\Psi < 3''$, and the red solid line shows components with $\Psi > 3''$. All three populations show a clear bimodal distribution with a peak at large angular separations that is dominated by random VLASS detections and a peak at smaller angular separations that mostly results from genuinely associated radio components (see also the radio two-point correlation function, e.g., Cress et al. 1996; Blake & Wall 2002; Gordon et al. 2021). Notably, the small angular separation peak constitutes a larger fraction of the population for extended components than it does for compact components. The relative positions of distribution peaks in Figure 3 is an effect of source density—lower on-sky densities will drive the nearest neighbor distributions to higher angular separations.

Even pairs of components with low angular separations will suffer some contamination from random associations. In order to improve the reliability of our data selection even further, we make use of the mean misalignment of the components in the pair relative to the axis of the pair (see Figure 4). Here, we define the mean misalignment as:

$$\Delta\theta_{\rm mean} = \frac{\Delta\theta_1 + \Delta\theta_2}{2}, \tag{1}$$

where $\Delta\theta_n$ is the relative misalignment (between 0° and 90°) of the position angle of component n, θ_n, relative to the position angle of the pair, $\theta_{\rm pair}$, given by:

$$\Delta\theta_n = |\theta_n - \theta_{\rm pair}|. \tag{2}$$

At larger angular separations, one would expect the components of the majority of true DRAGNs to be relatively well aligned with the pair axis, since the emission will arise from the originating jets or the trailing lobe structures.

In Figure 5 we plot the mean component misalignment of our pair sample as a function of pair separation, demonstrating that the antimode (local minima) of the pair separation distribution moves to smaller values as the misalignment of

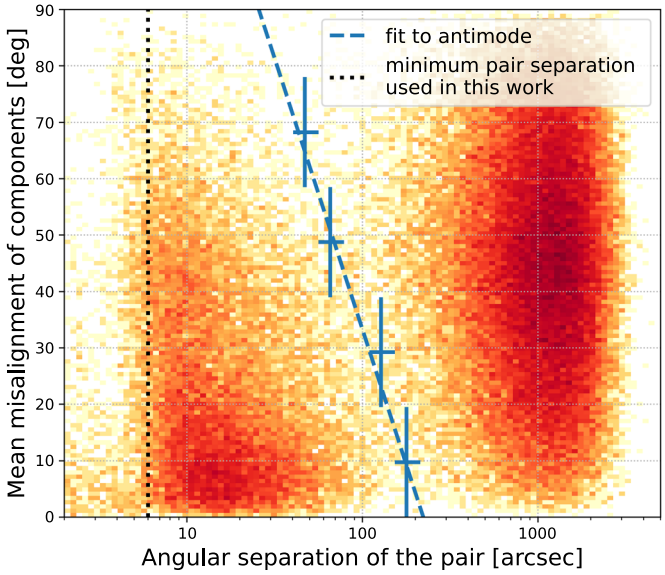

Figure 5. The mean misalignment of the lobes of candidate DRAGNs as a function of their angular separation. For component pairs separated by less than ≈200″ the components typically have position angles similar to the axis of the pair, whereas larger pairs show a random distribution of component alignments relative to the pair axis. The blue points highlight the pair separation antimodes for bins of mean alignment, the error bars on these points represent the bins used. The blue dashed line is a least-squares fit to the antimodes that we use to define a sample of likely real double radio sources (see Equation (3)). The black dashed line represents the minimum pair separation we use to select our DRAGNs in this work.

the pairs increases. Taking the antimode of the pair separation for pairs in different mean misalignment bins (blue crosses in Figure 5), we derive a linear fit given by:

$$\frac{\Delta\theta_{\rm mean}}{\rm deg} < -96.01 \log_{10} \frac{d}{\rm arcsec} + 225.32, \tag{3}$$

to aid in selecting real double sources (blue dashed line in Figure 5), where d is the angular separation of the pair components, and $\Delta\theta$ is the mean misalignment of the pair. Figure 5 shows that most of the pairs in the left-hand population have pair separations with

$$d > 6''. \tag{4}$$

A pair separation of 6″ is ≈2× the VLASS beam size and represents a clean separation of two extended components. The small population of pairs with $d < 6''$ do not follow the general trend of increasing mean misalignment with decreasing pair separation seen in the rest of the pairs, and likely represent pairings of components with poorly constrained measurements. We therefore select pairs satisfying Equation (3) and (4) as our DRAGNs. These criteria select 17,724 DRAGNs represented by data points to the right of the black dotted line and underneath the blue dashed line in Figure 5.

2.3. Core Finding

The key aspect of the double finding we perform is that it searches specifically for pairs of extended radio components. One necessary consequence of pre-selecting such candidate lobes is that compact components that may represent radio cores are initially excluded from association with the radio sources found by the pair finding. In order to attempt to recover

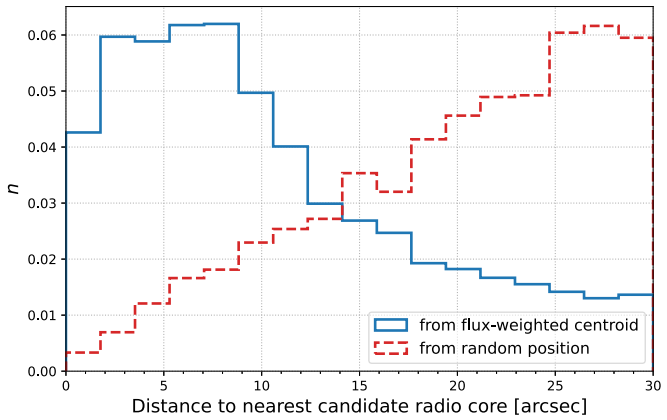

Figure 6. The normalized (by area under the lines) distributions of the angular distance to the nearest core candidate from the flux-weighted central position of the DRAGN (blue solid line), and from random sky coordinates (red dashed line).

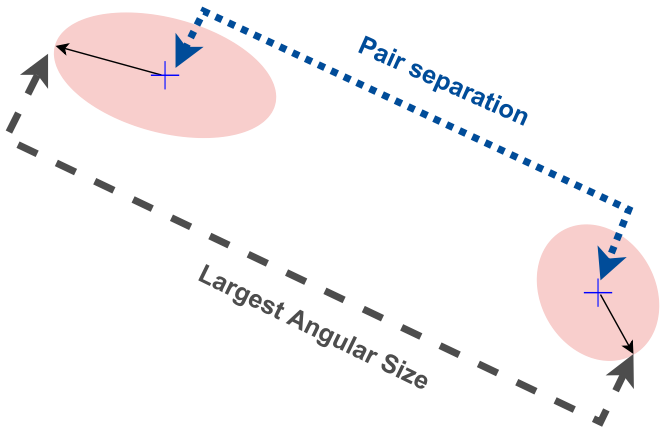

Figure 7. Schematic showing how we determine the LAS (gray dashed line) of our DRAGNs. The pink ellipses represent the geometry of the two lobe components after deconvolution from the VLASS beam. Our LAS measurement differs from the pair separation (blue dotted line) of the two lobe components by extending the pair size by the semimajor size of the components (black arrows) in the direction of the component position angle away from the pair center.

these missed cores, we search for candidate radio cores in the population of radio components that were not considered to be candidate radio lobes, i.e., $S_{\rm peak} > 3$ mJy beam^{-1} and $\Psi < 3''$. We search for such candidate cores within $30''$ or half the pair separation (whichever is the lesser) of the central position of our DRAGNs.

In ≈90% of cases, no core is found. Of the remaining 10%, only one core candidate is found in the majority of cases, with <1% of our candidate DRAGNs being associated with more than one core candidate. Visual inspection of DRAGNs with multiple core candidates shows these cases to generally be the result of sidelobes produced by bright sources. In Figure 6 we show the angular separation to the nearest candidate core from the flux-weighted centroid of the DRAGN (blue) and from a random sky coordinate (red). The random sky coordinates are obtained by subtracting 1° from the decl. of the real positions. Where core candidates are found, they are generally within $\approx 10''$ of the flux-weighted central position of the DRAGN. The strong peak in the core candidate distribution at small separations from the positions of the candidate DRAGNs is indicative of this sample being dominated by real DRAGNs with a detected core. In the rare cases where a DRAGN is associated with multiple core candidates, the closest candidate to the central position of the DRAGN is adopted as the core ID. In total, 1836 of our DRAGNs have a core identification.

Having identified all of the VLASS components associated with our DRAGNs, we also have a list of VLASS components that are not a part of any of our DRAGNs. Although some of these will be associated with more complex radio structures, the majority will be simple-morphology sources. For those components unaffiliated with any of our DRAGNs we select those with $S_{\rm peak} > 3$ mJy beam^{-1} as a reference set of single-component radio sources with which to compare our DRAGNs throughout the rest of this work. This sample contains 577,651 sources.

2.4. Key Measurements

With a catalog of DRAGNs in hand, we can derive key observable properties of the DRAGNs based on their constituent components. Perhaps the most fundamental property of any radio source is its total flux density, S. For our DRAGNs we estimate this by taking the sum of the total flux densities of all of the constituent components, i.e., $S_{\rm DRAGN} = S_{\rm Lobe\ 1} + S_{\rm Lobe\ 2} + S_{\rm Core}$.

Another essential measurement to make when characterizing DRAGNs is the largest angular size (LAS) of the radio source. To determine the LAS of a DRAGN, one could take the separation of the two lobe components as a proxy for the LAS. However, this would more accurately represent the distance between the radio component centroids rather than the full extent of the radio structure. A more robust approach would be to measure the angular extent subtended by the radio source above some signal-to-noise ratio (S/N) threshold. Such an approach would require making additional measurements from the image of the source rather than being easily calculable from the catalog data used by DRAGNHUNTER. Instead, we choose a compromise approach to estimate the LAS of our DRAGNs. We define the extreme coordinates of the radio double to be the lobe component coordinates offset by their semimajor axis size in the direction away from the pair center given by the lobe component position angles (see Figure 7), and take the distance between these coordinates to be the LAS. For our single-component sources, we take the LAS to be the measurement of deconvolved major axis size as listed in the component catalog. The distributions of integrated flux density and LAS for our DRAGNs are shown in Figure 8, demonstrating that larger DRAGNs are generally brighter.

3. Sample Reliability and Completeness

3.1. Reliability of DRAGN Detections

3.1.1. Overall Sample Reliability

In order to assess the reliability of our algorithm in selecting DRAGNs, a validation sample of 500 random DRAGNs is visually inspected. The errors reported on our fractional estimates (here, and throughout) are binomial uncertainties as described in Cameron (2011). Using our validation sample, we find that overall $89.0^{+1.2}_{-1.6}$% of the selected "DRAGNs" are genuine radio doubles, and example real DRAGNs identified are shown in Figure 9. Approximately 11% of the time the sources identified by DRAGNHUNTER are not the radio doubles the algorithm is designed

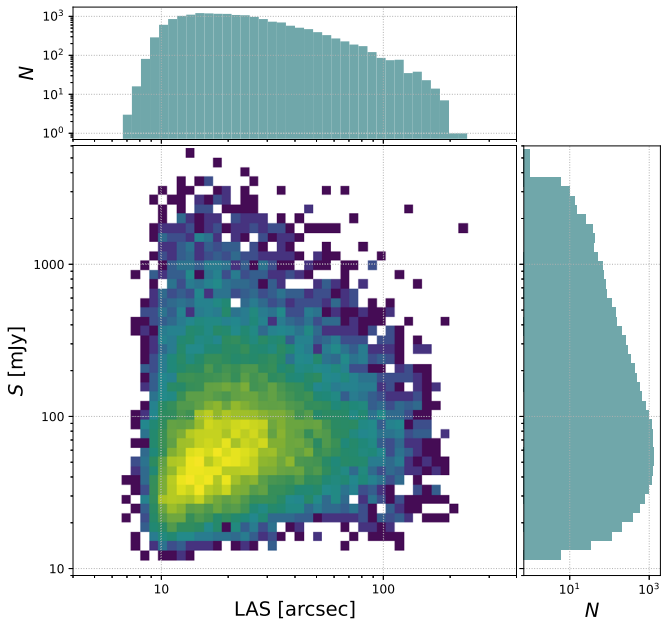

Figure 8. The distributions of LAS and integrated flux density (S) for our DRAGNs.

to select. This is to be expected given the range of complex radio morphologies that exist and the limitations of using only catalog data produced by a source-finding program rather than the image data directly.

There are three distinct types of spurious detections that DRAGNHUNTER produces. First, image artifacts (such as sidelobes around bright sources) can contaminate the component catalog used as an input for DRAGNHUNTER. Where this happens, these spurious detections can be selected as either one or both of the candidate lobes in a pairing of components (e.g., Figure 10(a)). Second, large diffuse structures that are not separate lobes of a DRAGN may be grouped together by DRAGNHUNTER. In Figure 10(b) we show an example where the two candidate lobes identified by DRAGNHUNTER are actually substructure within a single lobe of the DRAGN. Similarly, in Figure 10(c) we show a supernova remnant where DRAGNHUNTER mistakenly identifies part of the emission as two lobes of DRAGN. Third, in some cases a genuine lobe may be paired with an interloping candidate lobe (e.g., Figure 10(d)) because it is closer than the real counterpart. The risk of this type of false association increases with the angular size of the DRAGN. The on-sky density of candidate lobes (components with $S_{\rm peak} > 3$ mJy beam^{-1} and $\Psi > 3''$) is 3.5 deg^{-2}. For DRAGNs with LAS $< 30''$ (>70% of our sample), contamination from interloping candidate lobes is estimated to be <0.1%, while for DRAGNs with LAS $< 60''$ (>90% of our DRAGNs), this type of contamination rises to 0.3%.

3.1.2. Parameter Space Differences between Real and Spurious Detections

It is impossible to identify and remove all spurious detections without visual inspection of the entire catalog of >17,000 objects. However, knowing where DRAGNHUNTER fails allows for more robust selection criteria to be used in cases where sample fidelity is more important than sample completeness. Figure 11 shows comparative distributions (normalized by the area of the histogram) of a number of properties for genuine DRAGNs ($N = 445$) and spurious sources ($N = 55$) in our validation sample. For cases where DRAGNHUNTER is finding either part of a double (but not the whole) or the more complex morphologies of, e.g., supernova remnants, there is little reason to expect the components to be well aligned with the pair axis. Indeed, panel (a) of Figure 11 shows that spurious detections are more likely to have higher mean misalignments of their components: the median value of mean misalignment for genuine DRAGNs is 15°, while for spurious detections it is 35°. Selecting DRAGNs where the mean misalignment of the candidate lobes is $< 30°$ improves the sample reliability to $93.6^{+1.1}_{-1.6}$%. However, only ≈70% of our DRAGNs satisfy this criterion, so there is a cost in sample completeness.

Where unassociated components have been paired together by DRAGNHUNTER, there is no reason to expect the flux densities of the individual components to be correlated. Panel (b) of Figure 11 shows the distribution of S_1/S_2, where S_n is the flux of the component associated with lobe n. As expected, the spread of flux density ratios is larger for the spurious sources, where the standard deviation of $\log_{10}(S_1/S_2)$ is 0.98, than for genuine DRAGNs, which have a standard deviation of 0.34 in $\log_{10}(S_1/S_2)$. Nearly all of the genuine DRAGNs have components with flux densities within a factor of 10 of each other. Selecting only DRAGNs with $0.1 < S_1/S_2 < 10$ improves the reliability of the DRAGN selection to $92.6^{+0.8}_{-1.2}$%. Approximately 95% of the DRAGNs in our catalog have flux ratios lying in this range, making S_1/S_2 a very useful metric for identifying spurious sources.

The skew of the flux density distribution of spurious sources toward higher values relative to the sample of genuine DRAGNs shown in Figure 11(c) is consistent with contamination from bright source and sidelobe pairings. Such contaminating sources should also have small total angular extents. Figure 11(e) suggests most contaminants do in fact have relatively small values of LAS. However, while simply cutting sources with small angular sizes may improve the sample reliability, it will, of course, cut all of the genuine DRAGNs with small angular sizes as well. Figure 11(f) shows a cleaner distinction between genuine doubles and spurious detections in terms of the S/N of the LAS measurement. The median LAS/$\sigma_{\rm LAS}$ for genuine DRAGNs is ≈80, whereas for spurious detections it is ≈16. Approximately 94% of our catalog of DRAGNs have LAS/$\sigma_{\rm LAS} > 20$, and when only considering sources satisfying this criterion, the reliability of our validation sample is $95.8^{+0.8}_{-1.2}$%.

Both S_1/S_2 and LAS/$\sigma_{\rm LAS}$ can be used to produce higher purity samples of DRAGNs at a relatively small cost in sample completeness. Applying cuts in both of these parameters can improve the sample fidelity further still, while still only having a relatively low impact on the sample completeness. Of the DRAGNs in our catalog, 90% satisfy both $0.1 < S_1/S_2 < 10$ and LAS/$\sigma_{\rm LAS} > 20$. The reliability of such sources is estimated to be $97.5^{+0.5}_{-1.0}$% based on our validation sample. However, this estimate is based on a small number (55) of spurious detections in our validation sample. In order to confirm that the flux density ratio of the lobe components and S/N of the LAS estimate are indeed good metrics to select reliable DRAGNs, we randomly select a further 100 DRAGNs from our catalog that satisfy $0.1 \leqslant S_1/S_2 \leqslant 10$ and LAS/$\sigma_{\rm LAS} \geqslant 20$. Visually inspecting these 100 reveals two spurious detections, consistent with our

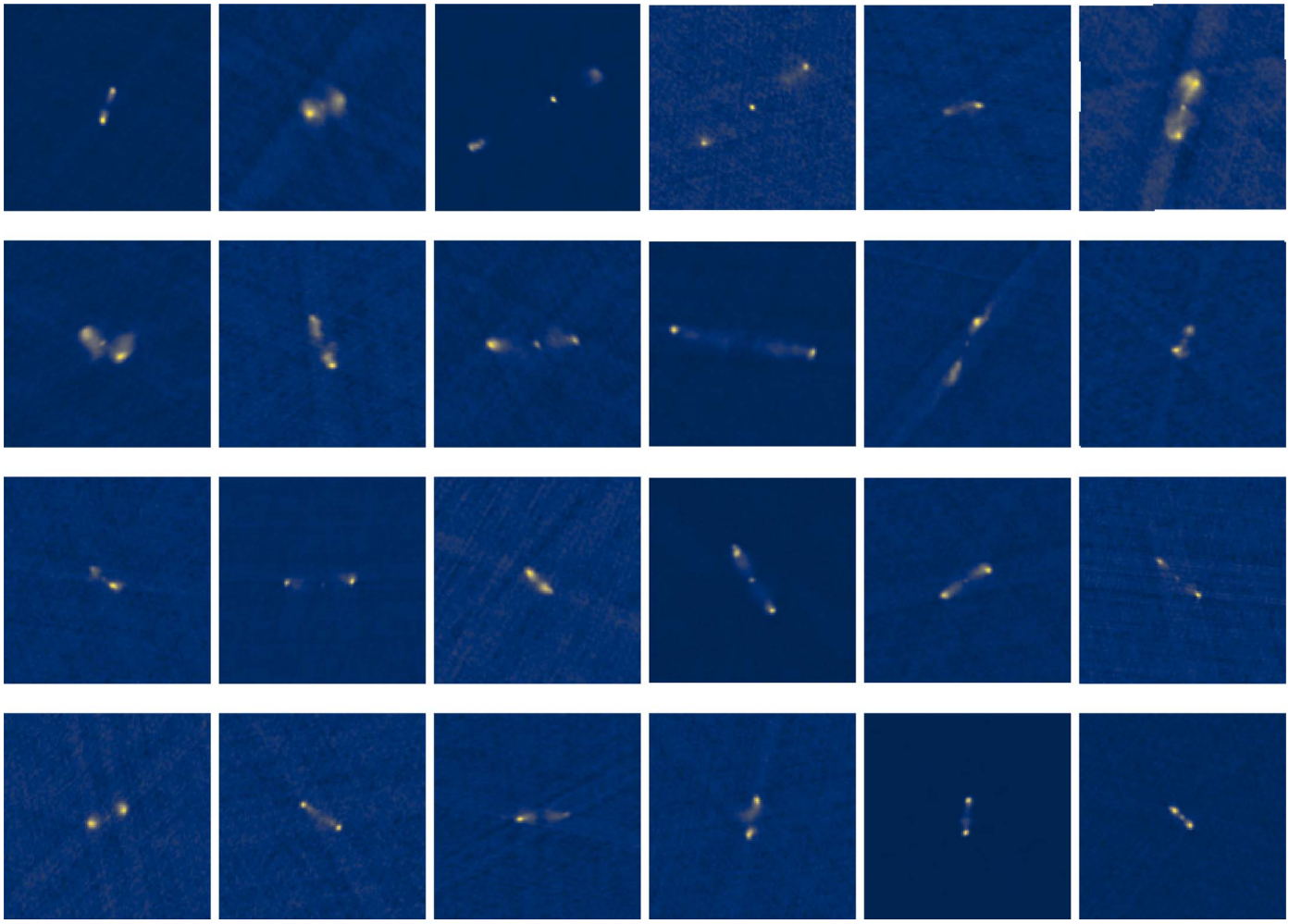

Figure 9. Postage stamp cutouts ($2' \times 2'$) of 24 examples of genuine DRAGNs. In many cases, a core is evident in the imaging even if not identified by DRAGNHUNTER, a result of our minimum 3 mJy beam^{-1} brightness threshold. Genuine radio doubles like these make up 89% of our DRAGN selection.

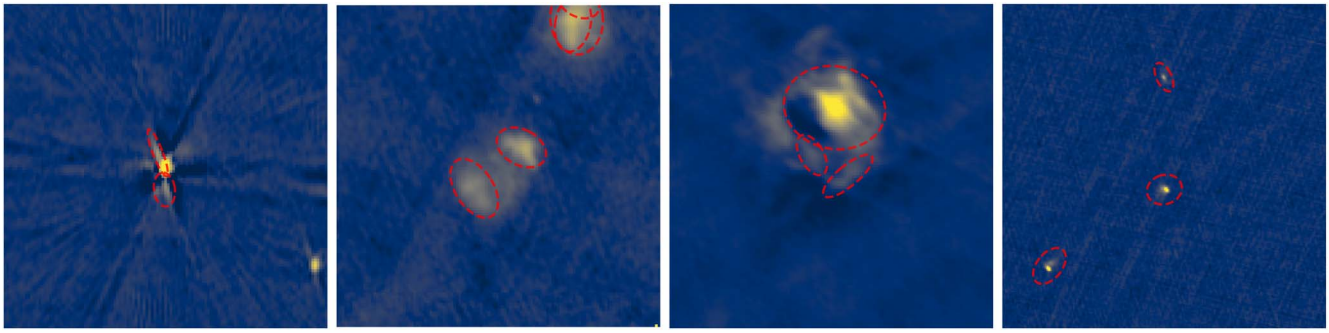

Figure 10. Four example postage stamp cutouts where DRAGNHUNTER has identified extended emission that is not the result of two distinct radio lobes. Panel (a) is a bright object with visible sidelobes where two of the sidelobes have been spuriously included in the component catalog and paired together by DRAGNHUNTER. In panel (b) part of an extended radio galaxy but not the whole source has been selected as a DRAGN. Panel (c) shows a supernova remnant where part of the continuum emission has been detected as multiple components. In panel (d), the component in the center and southeast of the image constitute a genuine DRAGN. However, in this case DRAGNHUNTER has paired the component in the center of the image with the unrelated component at the north of the image, as this is the closer pairing of candidate lobes. Panels (a)–(c) are $2' \times 2'$ cutouts while panel (d) is $4' \times 4'$. The red dashed lines show the position of components considered as candidate lobes by DRAGNHUNTER.

estimate based on our validation sample. In our catalog of DRAGNs we flag the ≈10% of entries with either $S_1/S_2 < 0.1$ or $S_1/S_2 > 10$ or $\mathrm{LAS}/\sigma_{\mathrm{LAS}} < 20$ as potential contaminants (see the catalog data model in the Appendix for details). This ability to select a large number of DRAGNs with high reliability will be of use to those wishing, for example, to create training sets for machine-learning algorithms designed to identify DRAGNs in radio images.

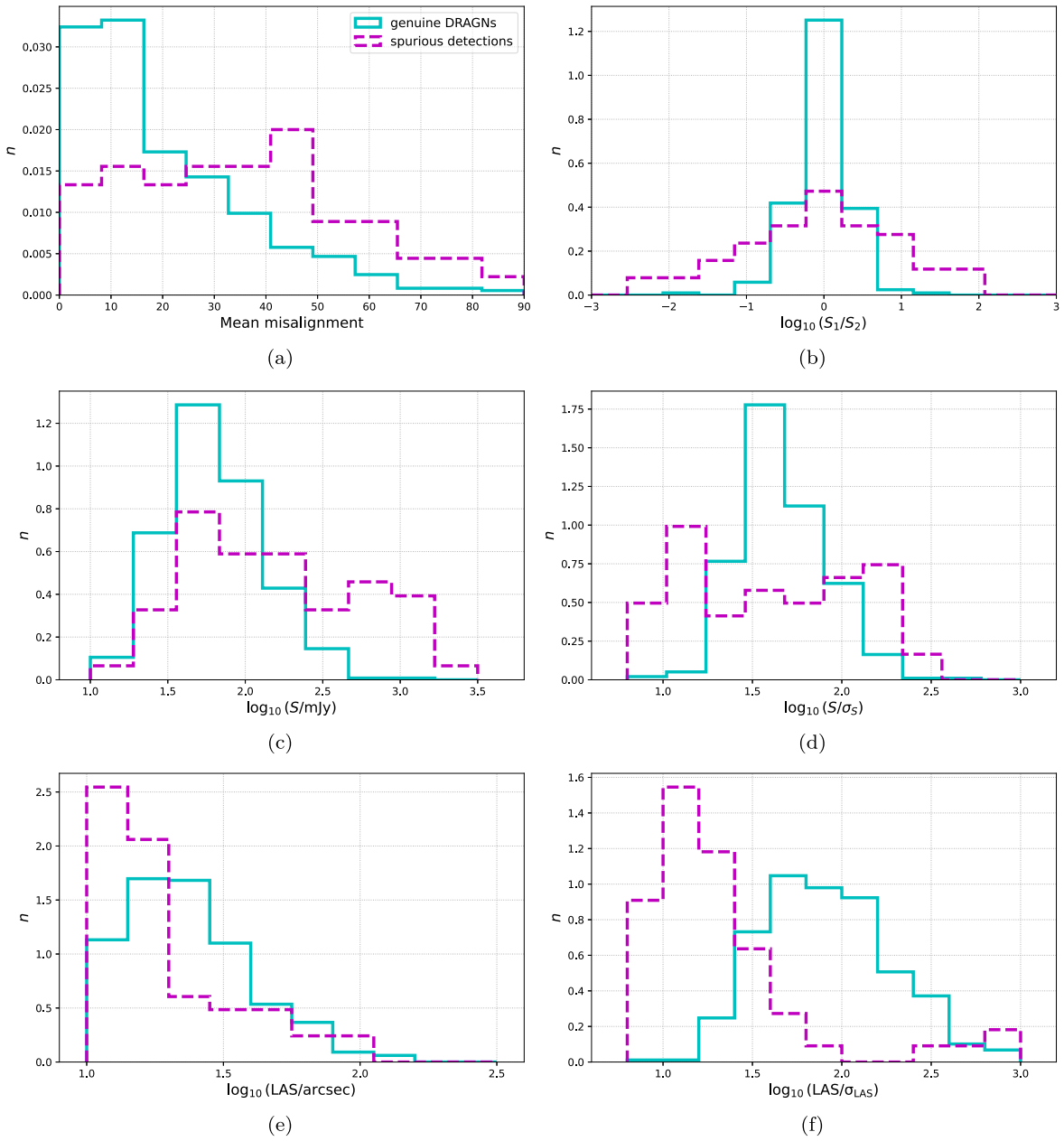

Figure 11. Distributions (normalized by area under the histogram) of mean component misalignment (a), component flux ratio (b), total source flux density (c), S/N in source flux (d), source LAS (e), and S/N in LAS (f) for sources identified as genuine (cyan solid line) and spurious (magenta dashed line) in our validation sample of 500 DRAGNs.

3.2. Sample Completeness

3.2.1. DRAGNs in VLASS Missed by DRAGNhunter

In order to check how well DRAGNHUNTER recovers DRAGNs from the VLASS data, 50 VLASS *Quick Look* images ($1^\circ \times 1^\circ$) with the cataloged components overlaid are visually inspected. This inspection reveals ≈2 DRAGNs per square degree that are visible in the image but not picked up by DRAGNHUNTER (examples given in Figure 12). Checking the catalog entries of such sources quickly demonstrates that in these cases one or both of the lobes have components that do not satisfy our original criteria for consideration as a candidate lobe (see Section 2.2). Panels (a) and (b) of Figure 12 show example "missing" DRAGNs where one component is identified as a candidate lobe (green ellipse) but the other has a peak flux density of <3 mJy beam^{-1} and is therefore too faint to be considered. Panels (c) and (d) of Figure 12 show example DRAGNs where both components have angular sizes of $<3''$ after deconvolution from the VLASS beam. These components are therefore too compact to be identified as candidate lobes in this work. All of the DRAGNs where both components satisfy the candidate lobe criteria in the 50 deg^2 of *Quick Look* images inspected are identified by DRAGNHUNTER.

DRAGNHUNTER thus does a good job at identifying brighter DRAGNs with clear extended lobes. Where DRAGNhunter fails is mostly on the fainter sources and those with smaller lobes. The fainter sources should be picked up more readily by relaxing the minimum brightness limit we employ in this work, and this may be appropriate for the *Single Epoch* VLASS images as they become available. The VLASS *Single Epoch*

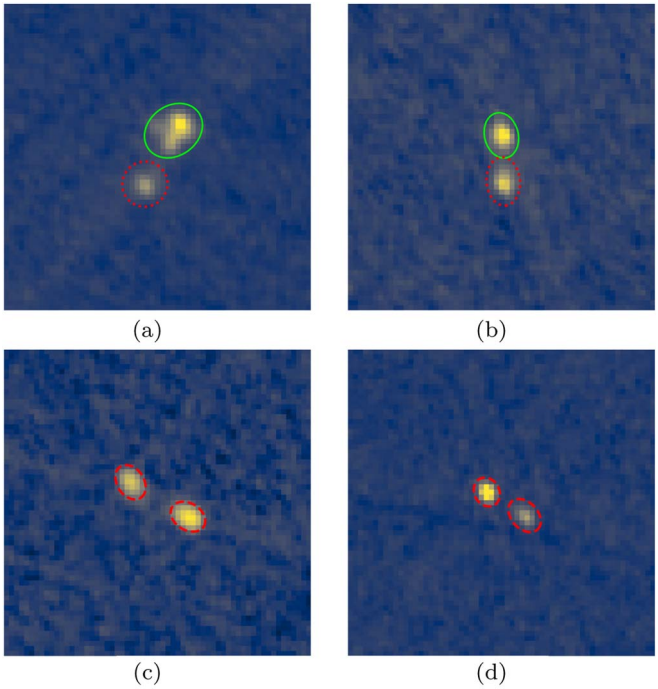

Figure 12. Example DRAGNs in VLASS not identified by DRAGNHUNTER. The overlaid components (colored ellipses) show why these examples are not selected by DRAGNHUNTER. Green ellipses with a solid line show components that satisfy the initial selection criteria as *candidate lobes* (see Section 2.2). Red ellipses are components that are not identified as *candidate lobes* either as a result of being too faint (dotted line) or too compact (dashed line). These postage stamps are $1' \times 1'$ and the ellipse sizes are set to $2\times$ the *fitted* component size for clarity.

images will be of a higher quality than the *Quick Look* images as a result of the use of self-calibration and deeper cleaning during image production (Lacy et al. 2022). Consequently, there should be fewer image quality issues at low S/N than in the *Quick Look* images.

3.2.2. Comparisons with Previous Catalogs

Estimating the completeness of our sample of DRAGNs requires a "ground truth" catalog of all of the existing DRAGNs that could be detected in the VLASS images at the sensitivities used by DRAGNHUNTER. As yet, such data does not exist. As an alternative, we compare the on-sky density of double sources identified here with other samples of doubles from the Faint Images of the Radio Sky at Twenty cm survey (FIRST; Becker et al. 1995) and the LOFAR Two Meter Sky Survey (LoTSS; Shimwell et al. 2017, 2019).

It is important to note that both FIRST and LoTSS are expected to capture more diffuse emission than VLASS because of the lack of short uv spacings in its VLA 3 GHz, B- and BnA-configuration data. In Figure 13 we show an example DRAGN as seen by VLASS, FIRST, and LoTSS. The LoTSS image clearly captures more extended emission than VLASS and even FIRST. Additionally, older lobes and plumes in DRAGNs are likely to have steeper spectra and will be preferentially missed at high frequencies. The integrated flux densities from the maps in Figure 13 correspond to $\alpha = -0.8$. If we instead use the fluxes from the component catalogs, we find steeper values, of $\alpha \approx -1.1$. In the following comparisons, we use a more conservative value of $\alpha = -0.7$ to scale between the surveys, but given the presence of steeper emission, especially in the component catalogs, and expected spectral curvature, the derived completeness values for VLASS likely represent a lower limit to the completeness for what should actually be visible in the 3 GHz radio sky.

For a comparison with FIRST, we extrapolate from Proctor (2011), who identified ≈90,000 double and triple sources. They used the 2003 April version of the FIRST component catalog (White et al. 1997; Becker et al. 2003) covering $\approx 9000\,\mathrm{deg}^2$ down to $S_{1.4\,\mathrm{GHz}} \approx 1$ mJy, for a source density of $\approx 10\,\mathrm{deg}^{-2}$. To compare this to the VLASS results, we first correct for the spectral index, assuming a typical spectral index for radio lobes of $\alpha = -0.7$. We then correct for the different sensitivities in the catalogs; 98% of our DRAGNs are brighter than 20 mJy (see Figure 8), corresponding to $S_{1.4\,\mathrm{GHz}} \gtrsim 34$ mJy, or 17 mJy per component. This represents only ≈10% of FIRST sources, leading to an expected source density of $\approx 1.16\,\mathrm{deg}^{-2}$ just over twice the DRAGNHUNTER source density of $\approx 0.51\,\mathrm{deg}^{-2}$. If we look at only the brightest DRAGNs, with $S_{3\,\mathrm{GHz}} > 100$ mJy, the corresponding densities are $0.17\,\mathrm{deg}^{-2}$ in VLASS using DRAGNHUNTER, compared to $0.20\,\mathrm{deg}^{-2}$ from Proctor (2011).

We also compared the DRAGNHUNTER source densities with those from LoTSS. Mingo et al. (2019) cataloged 3511 FR Is and FR IIs with $S_{150\,\mathrm{MHz}} \gtrsim 1$ mJy across $424\,\mathrm{deg}^2$. Again, using our $S_{3\,\mathrm{GHz}} = 20$ mJy comparison, this is equivalent to the 487 FR Is and FR IIs with $S_{150\,\mathrm{MHz}} > 163$ mJy. This corresponds to $1.15\,\mathrm{deg}^{-2}$, comparable to the above estimates from FIRST, and twice the density observed in VLASS. The corresponding numbers for $S_{3\,\mathrm{GHz}} > 100$ mJy are $0.28\,\mathrm{deg}^{-2}$ from Mingo et al. (2019), compared to the $0.17\,\mathrm{deg}^{-2}$ in VLASS.

Comparisons with data from both FIRST and LoTSS suggest that our catalog of DRAGNs is ≈45% complete at $S_{3\,\mathrm{GHz}} > 20$ mJy. At $S_{3\,\mathrm{GHz}} > 100$ mJy, we recover 85% of what we might expect based on FIRST, but only 60% of what the LoTSS numbers suggest, likely due to the combined effects of uv coverage, steeper spectrum emission than used in the calculations, and the nondetection of many FRI sources.

4. Multiwavelength Counterparts to Radio Sources

4.1. Host Candidates

To understand the physics underpinning the evolution of DRAGNs, it is necessary to identify the galaxy hosting the radio source. Not only does the multiwavelength cross identification provide information about the galaxy hosting the AGN, but it is essential in order to obtain a redshift estimate required to determine, e.g., the luminosity distance of the radio source. We search for potential counterparts to our DRAGNs that have been detected by the Wide-field Infrared Survey Explorer telescope (WISE; Wright et al. 2010), as WISE provides mid-infrared coverage of the entire sky. The typical point-spread function of WISE is 6.″1 in its bluest filter (W1, 3.4 μm), and an astrometric precision of better than 0.″5 is achieved even for faint sources. To this end, we use the AllWISE catalog (Cutri et al. 2012, 2013), which is around 95% complete at $\mathrm{W1} < 17.1$ mag (Vega) to identify host candidates for our DRAGNs.

We query the AllWISE catalog for sources within 30″ of the coordinates of the DRAGN. Where possible, the position of the radio core is taken as the coordinates of the DRAGN, but where a core has not been detected, we use the flux-weighted

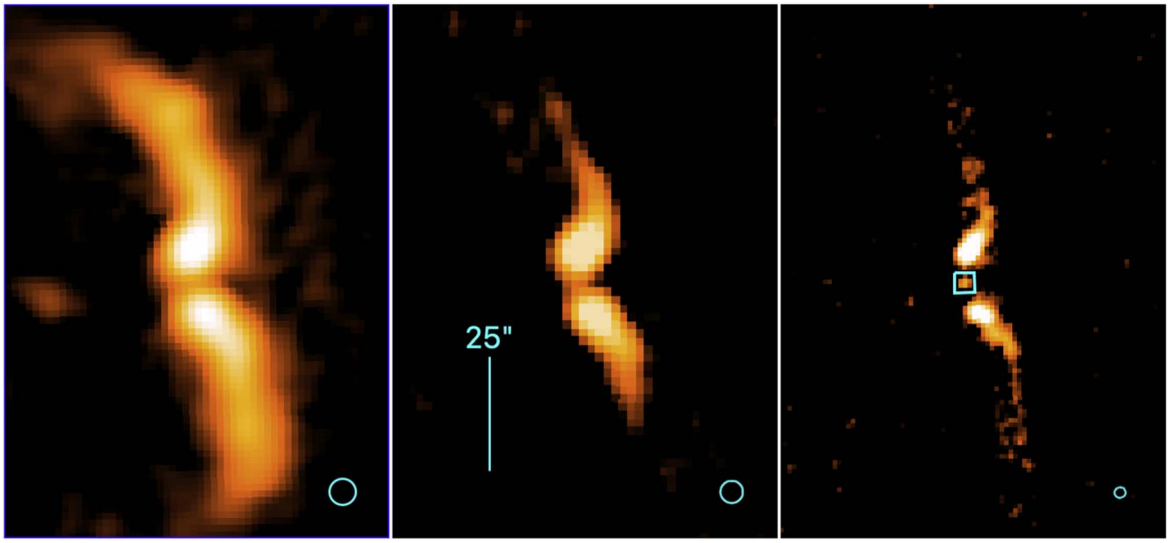

Figure 13. Radio images of the DRAGN J115915.34+491729.1 from LoTSS (left), FIRST (middle), and VLASS (right) on the same angular scale. The VLASS image shows the radio core (highlighted by the cyan box) that is not seen in the other two surveys, but misses the larger-scale low surface brightness emission seen clearly in LoTSS. The ellipse in the lower right of each panel shows the beam size and all of the images are log scaled. The images are each stretched until the background noise just becomes visible. The ranges are -0.6 mJy beam^{-1} to 135 mJy beam^{-1} (LoTSS), -0.1 mJy beam^{-1} to 12.3 mJy beam^{-1} (FIRST) and 0.46 mJy beam^{-1} to 3.1 mJy beam^{-1} (VLASS).

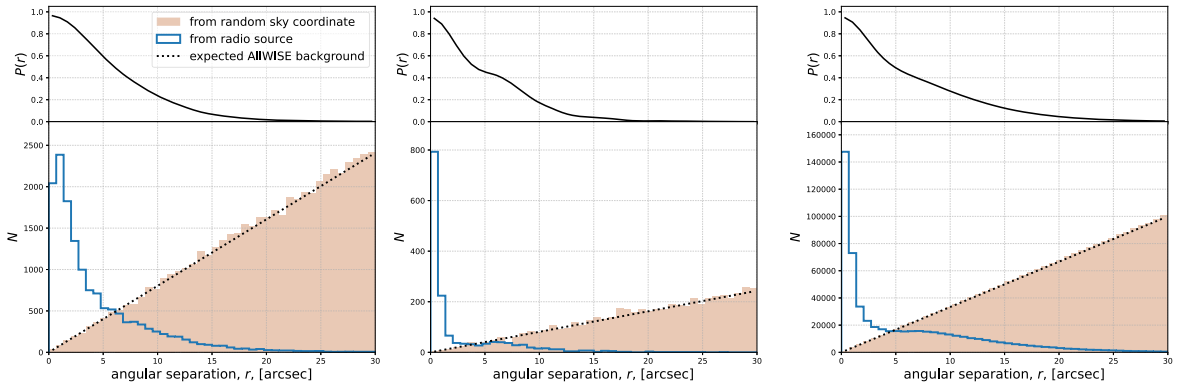

(a) DRAGNs (b) DRAGNs with cores (c) Single-component sources

Figure 14. The lower part of each panel compares the angular separation between radio sources and the nearest AllWISE source (blue solid line) and the number of AllWISE matches as a function of separation from the same number of random sky coordinates (pink solid histogram). The expected number of random matches given the AllWISE source density is shown as a black dotted line. The upper part of each panel shows the estimate of $P(r)$ determined by Equation (6) for this data. Panel (a) shows the comparison for our DRAGNs, panel (b) shows the same comparison only using DRAGNs with cores, and panel (c) shows the comparison done for single-component sources. The "hump" in the $P(r)$ curve at $r \approx 6''$ (most clearly visible in panel (b)) results from the typical separation at which the *nearest* random AllWISE match will be found.

central coordinates of the two lobes as there is an expectation for the brighter lobe to be closer to the host galaxy than the fainter lobe (de la Rosa Valdés & Andernach 2019; see also Section 6.1). In Figure 14(a) we show the angular separation to the nearest AllWISE source from our DRAGNs (blue solid line). For reference we show the number of sources detected when querying from random sky coordinates as a pink solid histogram, as well as the expected background count assuming the AllWISE source density (black dotted line). Following the approach outlined in Galvin et al. (2020), the expected background count, B, between given match offset radii, r and $r+dr$, using the AllWISE source density, $\rho \approx 17{,}000\,\mathrm{deg}^{-2}$, is estimated by:

$$B = N\ \rho\ 2\pi r\ dr, \tag{5}$$

where N is the number of coordinates being searched around.

For any particular angular separation, r, one can estimate an approximate probability, P, that a real match to the DRAGN will have such an angular offset by taking

$$P(r) = \frac{N_{\mathrm{match}}(r)}{N_{\mathrm{match}}(r) + N_{\mathrm{background}}(r)}, \tag{6}$$

where N_{match} is the number of genuine AllWISE associations with our DRAGNs, and $N_{\mathrm{background}}$ is the number of expected contaminating sources. In practice we approximate N_{match} at any given separation using the distribution shown in blue in Figure 14 and $N_{\mathrm{background}}$ using Equation (5). Crucially, by plotting $P(r)$, Figure 14 allows us to obtain a first-order approximation of the positional accuracy, σ_{pos} of our DRAGNs. Taking the FWHM of the $P(r)$ curve shown in Figure 14(a), we expect our DRAGNs to have a typical positional uncertainty of $\sigma_{\mathrm{pos}} \approx 6''$.

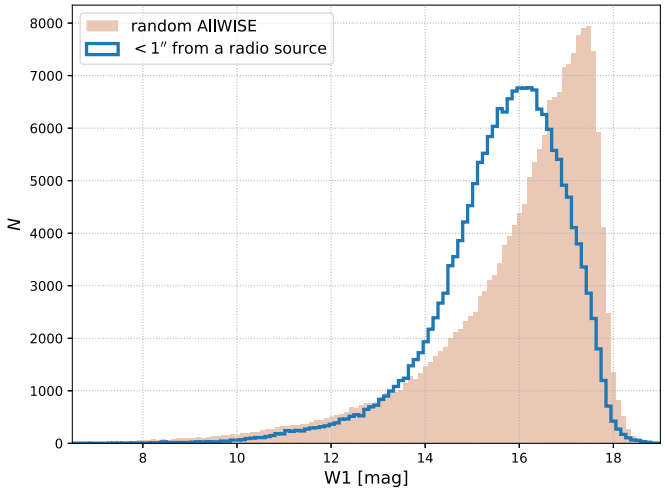

Figure 15. Distribution of W1-band magnitudes for AllWISE sources within 1″ of a radio source (blue solid line), compared to a random sample of AllWISE sources (pink solid histogram).

Figures 14(a) and (b) show the same comparison of angular separations to AllWISE sources shown in panel (a), but for DRAGNs with cores (panel (b)) and single-component sources (panel (c)). For single-component sources and DRAGNs with cores, the expected position of the host galaxy is known and the width of the $P(r)$ curve is driven by astrometric (im)precision. For DRAGNs where a core is not identified, the location of the host is less well constrained, and it is this lack of information rather than any astrometric imprecision that dominates the width of the $P(r)$ curve for DRAGNs. The adopted positional uncertainty for our DRAGNs thus represents the typical uncertainty in the location of the host for our sample of DRAGNs as a whole and not a hard limit on where we expect to find a host. In Section 4.2 we use this information to help identify the most likely host out of all potential candidates for each of our DRAGNs.

4.2. Likelihood Ratio Identifications

Taking the nearest AllWISE source to our DRAGNs may not be sufficient to identify the correct host. First, for any one radio/IR match, there is a (usually very small) possibility that the match is the result of a chance alignment of two unrelated sources. It is therefore helpful to know for any one match how likely it is to be a genuine association, and this can be better constrained by using information about the match beyond just its angular offset. For instance, the hosts of radio sources are typically brighter than the background AllWISE source distribution. We demonstrate this in Figure 15, which compares the W1 magnitudes of AllWISE sources within 1″ of a VLASS source to those AllWISE sources within 1″ of a random sky coordinate. Second, the source density of AllWISE is such that there may be multiple host candidates for each of our DRAGNs. Indeed, we show the distribution of the number of candidate AllWISE matches for our DRAGNs in Figure 16. For cases where multiple candidates are found, knowing the likelihood of each candidate to be the real match allows the best match to be selected.

One approach to finding the correct match between a radio source and an infrared (IR) source is to use the likelihood ratio (Sutherland & Saunders 1992; McAlpine et al. 2012). In short, this is the ratio of the probability that a matched source is the correct association, to the probability of that match being made by chance. These probabilities are determined using information (e.g., magnitudes, colors) about both the matched sources and background sources, as well as the angular separations between matches. Furthermore, the likelihood ratio is especially useful where poor resolution radio observations have multiple IR counterparts (McAlpine et al. 2012), which, to first order, is how we can treat our DRAGNs.

To identify the most probable hosts for our radio sources (both DRAGNs and single-component), we determine the likelihood ratio for all possible matches using the W1-band magnitude information for the AllWISE sources. Specifically, for this work, we define the likelihood ratio, LR by:

$$\mathrm{LR} = \frac{q(\mathrm{W1})f(r)}{n(\mathrm{W1})}. \quad (7)$$

Here, q(W1) is the probability that the radio source has an AllWISE counterpart with a given magnitude in the WISE W1-band, $f(r)$ is the radial separation probability distribution function for the cross match, and n(W1) is the sky distribution of AllWISE sources of a given W1-band magnitude.

To determine the LR, we adopt the approach detailed in Section 4 of Williams et al. (2019), with the exception of how we deal with positional errors. In Section 4.1 we estimated the typical positional uncertainty of our DRAGNs to be $\sigma_{\mathrm{pos}} = 6''$. However, this large positional uncertainty is unlikely to be appropriate for single-component sources. Here, the position of the host can be better constrained as, unlike for a pair radio lobes, the multiwavelength counterpart is generally coincident with the radio source. In order to account for this, we estimate $P(r)$ for single-component sources in a similar fashion to how $P(r)$ was estimated for our DRAGNs (see Figure 14(b)). For our DRAGNs, we determined the positional accuracy from $P(r) = 0.5$. As genuine AllWISE matches are expected to be spatially coincident with unresolved radio sources, we take a more conservative approach and determine the positional accuracy at $P(r) = 0.8$ to be $\sigma_{\mathrm{pos}} = 1\farcs8$.

Using a search radius of 30″ we query the AllWISE catalog to create a pool of likely matches to our radio sources. For sources smaller than $\approx 1'$, this search radius can result in candidates being considered that are not located between the two lobes. To counter this possibility, we additionally only consider matches with an angular separation of $r < 0.3$ LAS. For triple sources, the core component is found within 0.3 LAS of the flux-weighted centroid 90% of the time (see Figure 17), and we therefore consider that host candidates offset from the centroid of the DRAGN by more than 0.3 LAS are unlikely to be realistic candidates. For single-component sources, where $\sigma_{\mathrm{pos}} > 0.3$ LAS, we consider all matches with $r < \sigma_{\mathrm{pos}}$ to be realistic. Those matches we consider unrealistic are masked out from consideration before determining the LRs of the matches.

Knowing the LR for all possible AllWISE matches to a radio source, the reliability of any given match, R_i, is determined by:

$$R_i = \frac{\mathrm{LR}_i}{\sum_{j=1}^{N} \mathrm{LR}_j + (1 - Q_0)}, \quad (8)$$

for the match between the radio source and ith AllWISE candidate out of N possible matches. Here, Q_0 is an estimate of the fraction of radio sources with an AllWISE match (Fleuren et al. 2012) and for any given radio source $\sum_{i=1}^{N} R_i = 1$. For our sources, we adopt as the host ID the AllWISE matches with

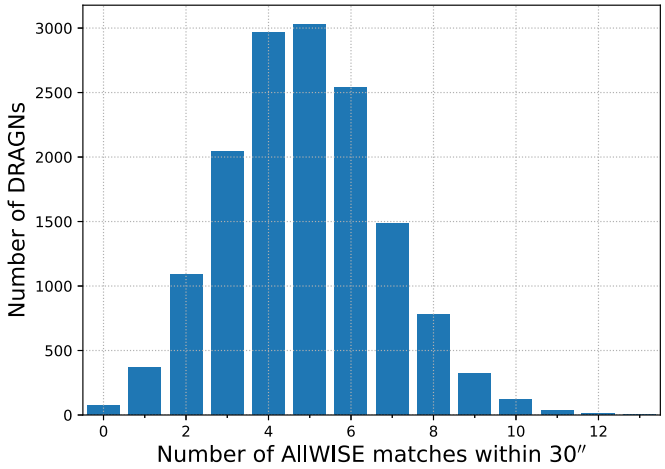

Figure 16. The distribution of the number of AllWISE matches found within 30″ of the flux-weighted centroid of the DRAGNs.

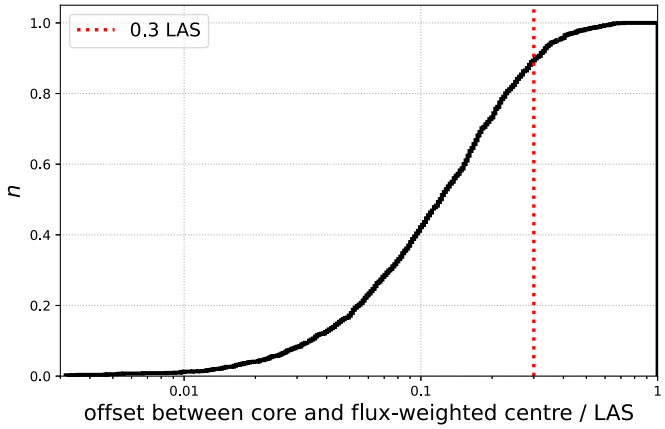

Figure 17. Cumulative distribution function (black solid line) of the angular separation of radio cores from the flux-weighted centroid of the two lobes normalized by the LAS for triple radio sources. The red dotted line shows the 0.3 LAS upper limit we use when finding AllWISE Host IDs for our DRAGNs.

reliability of $R > 0.5$. In Figure 18(a), we show an unblurred WISE (unWISE; Lang 2014) W1-band image for an example DRAGN with multiple AllWISE counterparts where the likelihood ratio has been useful in identifying the probable host.

4.3. Additional Information from Radio Cores

For the purposes of host identification, we have so far effectively treated our DRAGNs as though they were poorly resolved single-component sources. However, of the DRAGNs for which host candidates are identified, 1544 also have a radio core. Radio emission from a core will be spatially coincident with the AGN host galaxy. Thus, the core can be treated as an effective compact source and used to robustly identify the correct host. With this additional information in hand, we can assess the host IDs obtained from the likelihood ratio, and update these where necessary.

There are three possible scenarios where both a core and host have been identified independently of one another for a DRAGN. First, the core and host are colocated on the sky, which we define here as being separated by $< 1\farcs8$ (the same value as our adopted $\sigma_{\rm pos}$ for single-component sources). We find this to be the case for 1144 DRAGNs with both core and host identifications (74%), and accept these host IDs as being correct. Second, the core may be spatially coincident with an alternative host candidate, rather than the one with the highest likelihood ratio. We find this to be the case for 29 DRAGNs (2%). In such cases, we update the host ID to the candidate determined by the core. In panel (b) of Figure 18 we show an example where the likelihood ratio would suggest an incorrect host for the DRAGN. Here, the most likely candidate has $R = 0.59$ (gray dashed circle in Figure 18(b)). However, a radio core is coincident with one of the other host candidates ($R = 0.40$; green circle in Figure 18(b)), allowing us to confidently adopt this AllWISE source as the host for the DRAGN. Third, the core and host ID are not spatially coincident, and the core is not colocated with an alternative host candidate, e.g., as a result of the real host being too faint to be detected in AllWISE. For the 371 (24%) DRAGNs where this is the case, we do not trust the host ID and consider the source to have no AllWISE counterpart. It is also worth noting that the triple sources with misidentified hosts highlight the fact that the LR-derived host IDs represent the *most probable* host for each radio source and as such have a chance of being incorrect. To aid others in using our data, we include both the likelihood ratio and reliability for the host IDs in our catalog (see the Appendix for details).

Taking into account that 24% of the host IDs for triples are untrustworthy, reliable host IDs are found for ≈64% of triple sources. Assuming a similar global host reliability for the entire catalog of DRAGNs suggests that ≈55% of our ≈17,000 DRAGNs have robust host IDs. The apparent improvement in the cross ID rate when a radio core is present is likely the result of having a more precise starting point when searching for host candidates. Recall from Section 4.1 that for triple sources the position of the radio core is used to search for host candidates, whereas for double sources the flux-weighted centroid of the two lobes is used. The LR for any host candidate is a function of angular separation between the radio and IR sources—all other things being equal, a larger angular offset will result in a lower LR. One potential consequence of this is that a lower fraction of double sources than triple sources may have host candidates with $R > 0.5$. For example, in the case of a DRAGN with a radio core and three candidate hosts, if one of the host candidates is in fact the correct host, it will have a very small angular offset from the radio position. Consequently, the correct host will likely have a substantially higher LR value than the two other candidates that are at larger angular offsets, leading to a situation where the correct host has R close to unity and the other two candidates have $R \approx 0$. However, if the radio core had not been detected, then the additional uncertainty in the radio position can lead to cases where the closest two host candidates are separated from the flux-weighted centroid adopted as the radio position by several arcseconds. In cases where the host candidates also have similar magnitudes in the W1-band, this can result in multiple candidates having similar LR values such that even the most likely candidate has $R < 0.5$.

While the presence of a radio core can be used to confirm, update, or reject the LR-derived host IDs, this information was not used to determine the LR values. One might, therefore, ask whether there is any difference in the LR values between the

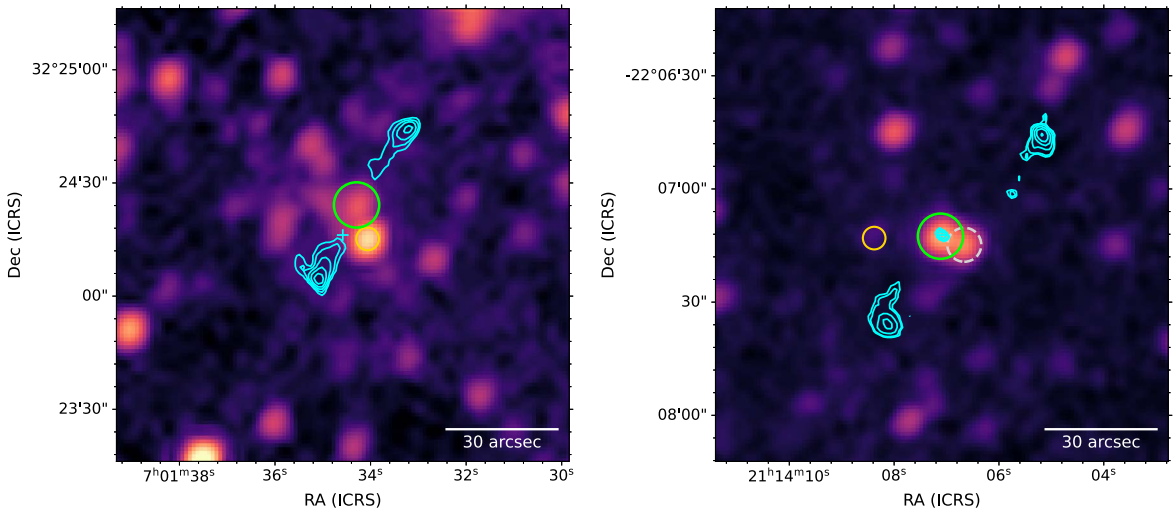

(a) (b)

Figure 18. Example unWISE W1-band images for DRAGNs where multiple host candidates are considered, showing the radio emission overlaid with cyan contours. Yellow circles are used to show AllWISE sources that are initially identified as being near the central position of the DRAGN (cyan cross) but are rejected as the host. The larger green circles show the adopted host. In panel (a) no radio core has been identified, and the host ID is selected as the most probable match from the likelihood ratio ($R = 0.75$). Panel (b) shows an example DRAGN where a core has been identified, and this information has been used to update the host ID. Here, the gray dashed circle shows the AllWISE source that the likelihood ratio has identified as the most probable match ($R = 0.59$) but that was replaced by the host candidate coincident with the radio core (green circle).

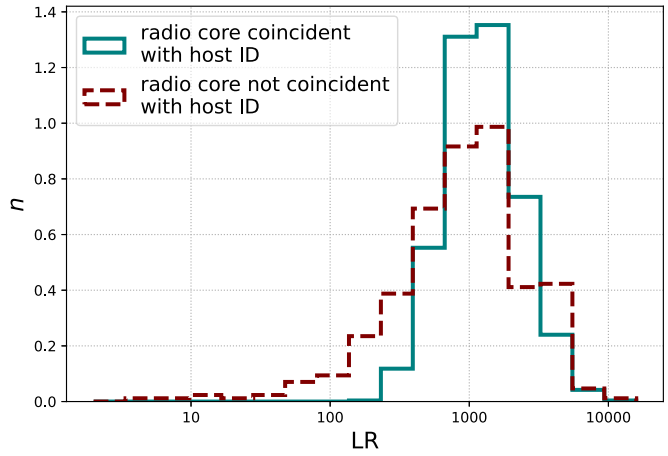

Figure 19. Comparison of the distributions of likelihood ratio values (LR) for triple sources where the host ID is spatially coincident with the radio core (teal solid line) and where the host ID is not colocated with the core (maroon dashed line).

host IDs where the core confirms the host, and those where the core information leads us to reject the host ID. In Figure 19 we compare the distributions of LR values for sources where the radio core and LR method agree (teal solid line) and disagree (maroon dashed line) on the host ID. Although high values of LR are found for both populations, there is a tail to lower LR values seen for sources where the LR-derived host ID and radio core are not spatially coincident that is not present for sources where these two approaches agree on the host. The median LR for sources where the core confirms the host is ≈1200, compared to ≈1000 for those where the core refutes the nominal host. Even though the LR approach may sometimes misidentify the correct host ID from the available candidates, the LR itself may be lower in such cases. Furthermore, it is notable that only for a small fraction of cases (7%) where the LR host ID was shown to be incorrect was an alternative host candidate identified by the core, suggesting that IR imaging depth is driving the misidentifications. Deeper IR (or optical) imaging relative to the radio depth is likely the key to improve the reliability of host identifications.

After updating the host information where appropriate in DRAGNs with a radio core, we identify likely hosts for 12,950 DRAGNs. Furthermore, on rechecking the validation sample (see Section 3.1) after performing the host finding, we note that the probability of DRAGNs in our catalog being genuine is higher than the overall reliability of the catalog at $93.1^{+1.1}_{-1.6}$% when a host is identified. This is probably the result of an IR counterpart between two real radio lobes being more likely than a random interloper between two associated radio sources at small angular separations. An additional 234,033 hosts are identified for the single-component sources.

4.4. Redshifts

4.4.1. Spectroscopic Redshifts

In order to determine physical properties such as the linear size and luminosity of our DRAGNs, we must first determine the redshift, and, by extension, the distance of these sources. Ideally, redshift is determined from spectroscopic observations of the host galaxy in order to get the most precise measurement. To identify spectroscopic redshifts (spec-zs) for our radio sources (both single-component and DRAGNs), we cross match the host IDs with a number of legacy catalogs of spectroscopic data. Namely, these are the Sloan Digital Sky Survey (SDSS; York et al. 2000; Blanton et al. 2017) Data Release 16 (DR16; Ahumada et al. 2020), the third data release of the Galaxy and Mass Assembly survey (GAMA; Driver et al. 2011; Baldry et al. 2018), the two-degree Field Galaxy Redshift Survey (2dFGRS; Colless et al. 2001), the six-degree Field Galaxy Survey (6dFGS; Jones et al. 2004, 2005), the WiggleZ survey (Drinkwater et al. 2010, 2018), and the Two Micron All Sky Survey (2MASS;

Table 1
Number of Redshifts Obtained from Different Redshift Surveys

Redshift Survey	$N_{\rm DRAGNs}$	$N_{\rm single\text{-}component}$	$N_{\rm total}$
SDSS DR16	1150	26,968	28,118
6dFGS	76	2513	2589
2MRS	28	1205	1233
WiggleZ	22	356	378
2dFGRS	9	341	350
GAMA	1	92	93
LS DR8 (photo-zs)	2552	51,536	54,088

Skrutskie et al. 2006) Two Micron Redshift Survey (2MRS; Huchra et al. 2012). Overall we find spec-zs for 32,761 sources, 1286 of which are for DRAGNs.[13] A full breakdown of how many spec-zs are obtained from each survey is given in Table 1.

4.4.2. Photometric Redshifts

While spectroscopic measurements are preferred for determining redshift, the time and expense of obtaining spectra means that the vast majority of radio galaxies—and more than 90% of our DRAGNs—have not yet been observed in this manner. In these cases, photometric redshifts (photo-zs) can provide an alternative to spec-z measurements. As these are based solely on imaging data, photo-zs are often available for a much larger number of sources than spec-zs are, and are now frequently produced for wide-field imaging surveys (e.g., Beck et al. 2016, 2021; Zhou et al. 2021).

In order to increase the number of DRAGNs in our sample with redshifts, we cross match our hosts that do not have a spec-z with Data Release 8 of the Dark Energy Survey Spectroscopic Instrument (DESI) imaging Legacy Surveys (LS DR8; Dey et al. 2019) photo-z catalog (Duncan 2022). The Duncan (2022) LS DR8 photo-zs are determined by Gaussian mixture models (GMMs; Bovy et al. 2011) making use of optical and infrared photometry from the g-, r-, z-, W1-, and W2-bands. Importantly for this work, the GMM derived photo-zs for LS-DR8 have been demonstrated to be more reliable for RLAGNs than other alternative photo-zs for the DESI imaging Legacy Surveys (Duncan 2022). Cross matching with the Duncan (2022) LS DR8 photo-z catalog provides an additional 51,536 and 2552 redshifts for our single-component sources and DRAGNs, respectively. In total, 83,011 single-component sources and 3838 DRAGNs have either a spec-z or photo-z measurement available (≈30% of sources with a host). The distributions of the collated redshifts are shown in Figure 20 split by redshift type (spec- or photo-z).

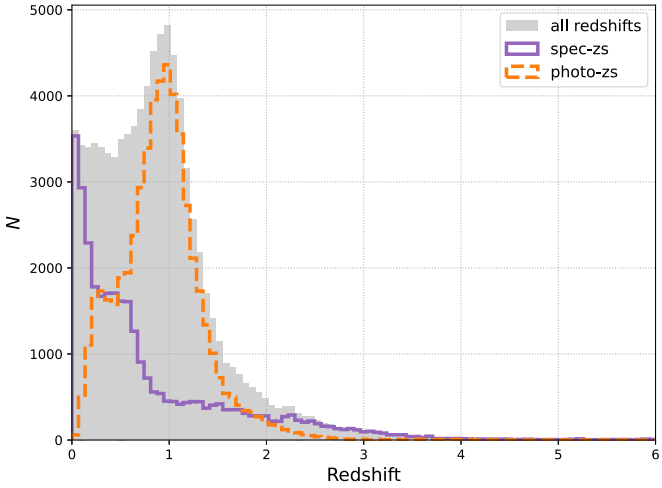

Figure 20. The redshift distribution of our radio sources (single-component and DRAGNs). The gray histogram shows all redshifts, spec-zs are shown by the purple solid line, and the orange dashed line shows photo-zs.

5. Properties of the DRAGN Population in VLASS

5.1. The Sizes and Luminosities of DRAGNs

We now turn to exploring the properties of the DRAGN population. One of the most important properties of a radio galaxy is its luminosity. For the DRAGNs where we have obtained a redshift, we calculate their 3 GHz luminosity. The flux density measurements used for this are scaled up by a factor of $1/0.87$ in order to account for the systematic flux under-measurement in the VLASS epoch 1 *Quick Look* component catalog (for a detailed description, see Gordon et al. 2021). Radio source luminosities are often compared to their projected largest linear size (LLS) on a power versus diameter (P–D) diagram (e.g., Baldwin 1982; Blundell et al. 1999; An & Baan 2012; Hardcastle et al. 2019; Mingo et al. 2022). We determine the LLS for our DRAGNs and show them on a P–D diagram in Figure 21. For comparison, we additionally show the linear size and luminosity distributions of single-component sources, excluding the unresolved "zero size" sources.

The DRAGNs are generally higher-power sources than their single-component counterparts by nearly an order of magnitude, with a median 3 GHz luminosity of $10^{26.5}$ W Hz^{-1} compared to $10^{25.7}$ W Hz^{-1} for single components. On the P–D plane, our DRAGNs occupy a region typically inhabited by FR II radio galaxies (see, e.g., Figure 7 of Jarvis et al. 2019, Figure 5 of Mingo et al. 2019, or Figure 2 of Hardcastle & Croston 2020). It has been shown using LoTSS that some low-luminosity FR IIs occupy the regions of P–D space classically dominated by FR Is (Mingo et al. 2019), suggesting that these populations are not cleanly segregated on the P–D diagram. LoTSS is a low-frequency survey with high sensitivity to low surface brightness emission. Conversely, VLASS is a high-frequency survey, and the B- and BnA-configurations used by the VLA for VLASS observations lack the short baselines needed for sensitivity to diffuse emission. The resultant selection effects inherent to VLASS, as well as DRAGNHUNTER's strategy of requiring distinct components for each lobe, likely bias our DRAGNs toward those dominated by hotspots rather than the diffuse emission seen in FR Is. While we have made no attempt at a more in-depth morphological classification of our DRAGNs in this work, the examples shown in Figure 9 would also suggest our DRAGNs mostly appear as FR IIs in VLASS.

The DRAGN population appears to be consistent with an extension of the single-component source population on the P–D diagram such as would be expected from older and/or more intrinsically powerful radio jets (Hardcastle et al. 2019; Gürkan et al. 2022). However, while this may be true *on average* from a population perspective, inferring jet ages and powers for *individual sources* on the P–D diagram is complicated by

[13] For sources where we do not find a spec-z in the legacy catalogs that we check, smaller legacy catalogs or the wider literature may be able to provide spec-zs in some cases.

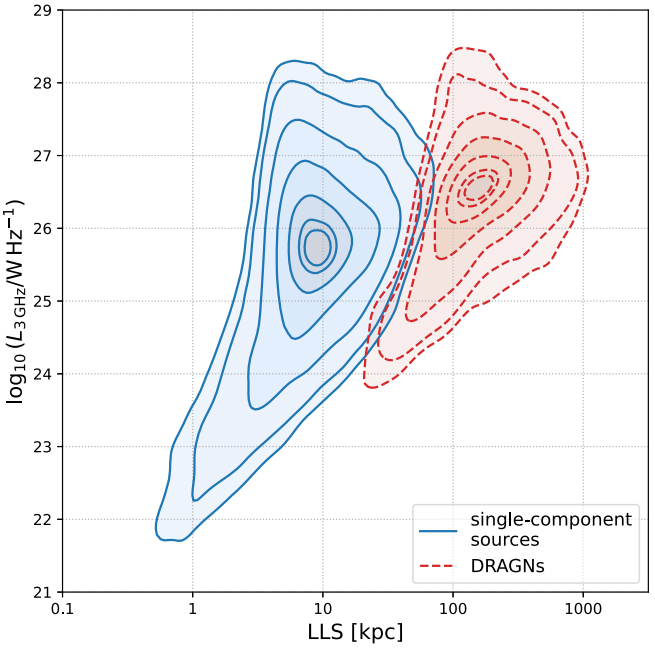

Figure 21. The linear size vs. luminosity plot (a *P–D* diagram) for our DRAGNs (red dashed contours) and single-component sources (blue solid contours). The contour levels contain 5%, 10%, 25%, 50%, 75%, 90%, and 95% of each data set.

factors such as host galaxy environment, and jet orientation effects (e.g., An & Baan 2012; Hardcastle & Krause 2013, 2014; Harwood et al. 2020). The absence of sources in the lower-right of the *P–D* plane is not a real effect, and rather is driven by surface brightness limitations of the survey images (Hardcastle et al. 2016; Hardcastle & Croston 2020).

5.2. Giant Radio Galaxies

Giant radio galaxies (GRGs) are some of the largest structures in the universe, reaching projected linear sizes larger than 700 kpc, and GRGs up to 5 Mpc in length have been reported (Willis et al. 1974; Bridle et al. 1976; Ishwara-Chandra & Saikia 1999; O'Dea et al. 2001; Dabhade et al. 2017; Oei et al. 2022). Identifying the largest radio galaxies is important in order to aid our understanding of the physics of jet propagation and aging. These galaxies typically have large angular extents, ranging from arcminute to degree scales (Cotter et al. 1996; Schoenmakers et al. 2001; Kuźmicz et al. 2018), and are often best identified in surveys at low frequency and that are sensitive to extended, low surface brightness emission. The survey design of VLASS, a relatively high-frequency survey utilizing the VLA's B- and BnA-configurations, which lack short baselines, is thus not optimized for finding GRGs. Nonetheless, given that we have linear size measurements for more than 3000 DRAGNs, we check our catalog for any GRGs that might have been found by VLASS.

For DRAGNs in our catalog listed as having LLS $>$ 700 kpc, we select only those with a likelihood ratio derived host reliability $>$ 0.8 or a radio core detection coincident with the host. These criteria select 43 candidate GRGs, which we visually inspect to confirm their nature. Of the 43 DRAGNs selected as likely GRGs, we reject four (9%) as being contaminants in our DRAGN sample. Eight further DRAGNs (19%) are rejected as the host ID is either incorrect or uncertain upon visual inspection. Two of the DRAGNs rejected as GRGs have substantially lower likelihood ratios for their host IDs (LR $\sim$ 5) than the rest of the GRG candidates (LR $\sim$ 1000). For the other rejected candidates, the likelihood ratio values were comparable to those confirmed by visual inspection. The numbers of rejected candidate GRGs are unsurprising given the overall sample reliability (Section 3.1) and the expected failure rate of the host IDs (Section 4.3). This leaves us with 31 GRGs, which we list in Table 2. Two of the GRGs, J003022.33-090107.0 and J015717.54+284734.8, have projected linear sizes greater than 1 Mpc.

We cross match our 31 GRGs with a number of existing GRG catalogs, namely:

1. A compilation of 349 GRGs from the literature by Kuźmicz et al. (2018);
2. 272 GRGs identified by Kuźmicz & Jamrozy (2021) in the NRAO VLA Sky Survey (NVSS Condon et al. 1998) and SDSS;
3. 162 GRGs identified by the Search and Analysis of Giant radio galaxies with Associated Nuclei (SAGAN) project (Dabhade et al. 2020a);
4. more than 2200 GRGs in LoTSS (Dabhade et al. 2020b; Oei et al. 2023); and
5. 55 GRGs in the ROGUE I (Radio sources associated with Optical Galaxies and having Unresolved or Extended morphologies I) catalog (Kozieł-Wierzbowska et al. 2020).

A catalog of GRGs in RACS (Andernach et al. 2021) contains an additional 178 GRGs, but this catalog is limited to $\delta < -40^\circ$ and therefore does not overlap with VLASS. In combination, these data sets provide a comprehensive list of all of the previously reported GRGs. None of our 31 GRGs are identified in the above data sets, suggesting that these are indeed newly discovered giants. It is likely that these GRGs were not previously identified as such due to a lack of host IDs and/or redshift measurements.

These 31 GRGs have been discovered despite neither VLASS nor DRAGNHUNTER being optimized to find sources with very large, multiarcminute scale, angular extents. In this work we have identified hosts and redshifts from existing survey data using an automated procedure, and more GRGs may be found by using the cataloged DRAGNs as a starting point for more thorough search. For instance, using our adopted cosmology, 700 kpc will always correspond to LAS $> 80''$. In our catalog 576 DRAGNs have such large angular sizes, but we have only identified redshift measurements for 124 of these. It is possible that at least some of the 452 remaining GRGs with LAS $> 80''$ may have redshift measurements available from legacy data we have not searched, either from the literature or additional surveys such as the Panoramic Survey Telescope and Rapid Response System (Pan-STARRS) survey (Chambers et al. 2016). Alternatively, further GRGs may be identified by relaxing the size criteria used by DRAGNHUNTER to reduce contamination from spurious "double source" detections. Such a dedicated search for GRGs is beyond the scope of this work, but presents tantalizing opportunities for future studies of the largest radio galaxies.

5.3. The Host Galaxies of DRAGNs

Knowing the AllWISE counterparts to our radio sources provides information on the galaxies themselves that host the AGNs. A common diagnostic plot for IR sources is the WISE

Table 2
Newly Discovered Giant Radio Galaxies in VLASS Identified by DRAGNHUNTER

Name	Flux Density[a] (mJy)	LAS (arcseconds)	Redshift	Redshift Type	$\log_{10} L_{3\,\mathrm{GHz}}$ (W Hz^{-1})	LLS (kpc)
J002506.84−342644.8	71.2	88	0.995	photo	26.78	700
J003022.33−090107.0	34.2	169	1.448	photo	26.92	1428
J003758.39−043651.5	23.3	118	0.524	photo	25.53	736
J010324.26+313216.6	45.4	92	1.193	spec	26.8	761
J011018.20−361711.5	35.8	92	1.005	photo	26.49	739
J013035.90−190120.1	73.0	90	1.036	photo	26.84	728
J013651.68+004055.7	55.2	94	0.83	photo	26.44	717
J013907.23−373323.1	99.2	117	0.772	photo	26.61	865
J015717.54+284734.8	108.7	137	0.841	photo	26.75	1043
J040701.36−315214.1	274.5	111	1.013	photo	27.38	894
J081740.34+294920.2	28.0	98	1.1	photo	26.49	798
J091452.88+225533.8	98.1	96	0.778	photo	26.62	714
J100749.11−045335.1	142.2	108	0.639	photo	26.54	744
J101718.07+393127.9	329.8	138	0.531	spec	26.69	869
J102214.84+174647.8	79.3	116	0.526	spec	26.06	728
J105304.35+312606.8	66.5	96	0.855	photo	26.56	736
J134817.65+055743.0	116.0	107	1.046	photo	27.05	867
J141622.01+590019.5	76.7	137	0.557	spec	26.12	882
J144925.52+221206.6	64.1	130	0.592	photo	26.11	862
J150558.82−061609.6	50.6	127	0.598	photo	26.02	847
J153230.42+241529.5	192.4	133	0.564	spec	26.53	865
J154057.76+171720.9	37.6	116	0.79	photo	26.22	867
J165037.20+324218.0	112.9	128	0.516	photo	26.19	796
J224402.55−095126.3	70.2	86	1.174	photo	26.97	711
J224430.84+265234.0	58.6	99	0.857	photo	26.51	759
J232458.76+280329.3	353.5	111	0.898	photo	27.35	863
J233451.89+080544.7	106.3	114	0.873	photo	26.79	882
J233753.38−143515.4	226.9	100	0.698	photo	26.85	711
J233855.71−105924.4	47.6	99	1.491	photo	27.1	840
J235725.34−113242.8	95.0	91	0.864	photo	26.73	705
J235811.70−083114.3	267.4	120	0.637	photo	26.81	828

Note.
[a] The flux density measurements presented in this table are higher than the cataloged values by a factor of 1/0.87 in order to account for the systematic underestimation of flux densities in the VLASS *Quick Look* component catalog (see Section 3 of Gordon et al. 2021). It is these values that have been used to estimate the radio luminosities.

(This table is available in machine-readable form.)

color–color diagram that compares the W1 − W2 color to W2 − W3 color, where the WISE W1, W2, and W3 filters are centered on wavelengths of 3.4 μm, 4.3 μm, and 12 μm, respectively. To this end, we select radio sources with reliable WISE magnitudes, i.e., those with S/N > 3 in the W1, W2, and W3 bands. Additionally, so as not to include objects where the photometry may suffer from blending in the high-density galactic plane, we exclude sources with low galactic latitudes, $|b| < 10^{\circ}$ (approximately 8% of our sources with host IDs lie this close to the galactic equator).

The single-component radio source sample may also contain blazars and star-forming galaxies, as well as the smaller angular scale radio galaxies with which we wish to compare our DRAGNs. Likely blazars are removed by only selecting sources with LAS > 3″, i.e., those that are clearly resolved by VLASS. Contamination from likely star-forming galaxies is addressed by only including sources with $L_{3\,\mathrm{GHz}} > 10^{23}$ W Hz^{-1}. Assuming a typical spectral index of $\alpha = -0.7$, in order to produce 3 GHz luminosities higher than 10^{23} W Hz^{-1} in the absence of an AGN, the host galaxies would require star formation rates in excess of 100 $M_{\odot}$ yr^{-1} (Bell 2003). Consequently, we can be confident this population is dominated by RLAGNs.

The WISE color–color diagram is most useful at $z < 1$ as the WISE bands start to trace different parts of the host galaxy SED at higher redshifts (Donley et al. 2012; Assef et al. 2013). Limiting our sample to those sources at $z < 1$, we identify 888 DRAGNs and 1422 single-component radio sources that satisfy our selection criteria. A further 316 DRAGNs and 697 single-component sources have either poor S/N or a lower limit in their W3 magnitude measurement and are not included in this analysis. We plot the WISE colors of the hosts of these RLAGN in Figure 22, showing DRAGNs in the upper panel and single-component sources in the lower panel. For our comparison of the IR colors of extended single-component radio galaxies and DRAGNs, we adopt the Mingo et al. (2016) classification of WISE host galaxies. Broadly, these criteria provide two different diagnostics. First, whether the IR colors are dominated by the AGN (W1 − W2 > 0.5) or the host galaxy (W1 − W2 < 0.5). Second, for those sources where the host galaxy dominates the IR colors, the W2 − W3 color provides information on the host galaxy type, as follows:

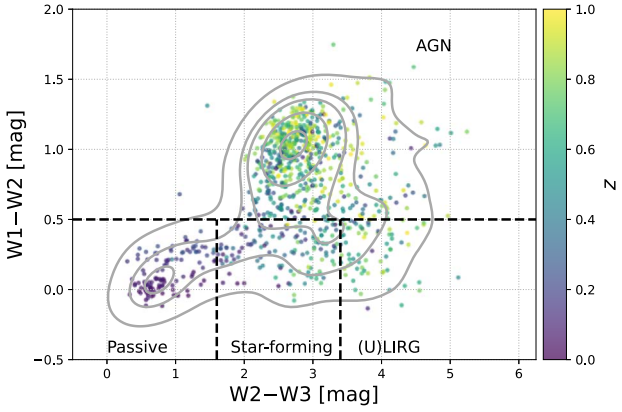

(a) DRAGNs

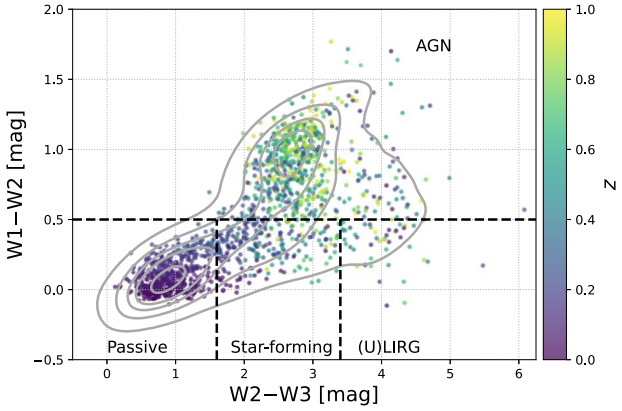

(b) Single-component sources (LAS > 3″)

Figure 22. The WISE color–color distributions for the hosts of DRAGNs (panel (a)) and extended (LAS > 3″) single-component radio sources (panel (b)). The contour levels contain 95%, 75%, 50%, 25%, and 5% of the data points, and all points are colored by the redshift of the host galaxy. Only galaxies with S/N > 3 in W1, W2, and W3 are included.

1. passive and elliptical galaxies generally have $W2 - W3 < 1.6$,
2. galaxies with $1.6 < W2 - W3 < 3.4$ are typically disk dominated and have more active star formation, and
3. sources where $W2 - W3 > 3.4$ are usually starburst galaxies, often (ultra) luminous infrared galaxies ([U] LIRGs).

Figure 22 shows some differences between the IR color distributions of the DRAGNs and extended single-component radio sources. For the DRAGNs, $65.2\% \pm 1.6\%$ have hosts with AGN-like colors, $12.3^{+1.2}_{-1.0}\%$ are passive, $14.6^{+1.3}_{-1.1}\%$ have star-forming colors, and $7.9^{+1.0}_{-0.8}\%$ are (U)LIRGs. This dominance of AGN IR colors with a nearly even mix of passive and star-forming hosts when the AGN does not dominate the IR closely resembles the WISE colors seen in previous works studying powerful extended radio galaxies (e.g., Gürkan et al. 2014; Banfield et al. 2015; Mingo et al. 2019). However, in the case of the single-component sources, when the IR colors are not AGN-like, there is a bias toward passive hosts. Here, $45.3\% \pm 1.3\%$ have hosts where the AGN dominates the IR colors, $34.7^{+1.3}_{-1.2}\%$ have passive colors, $16.7^{+1.0}_{-0.9}\%$ are star-forming galaxies, and for $3.2^{+0.5}_{-0.4}\%$, the hosts have IR colors associated with (U)LIRGs. The scatter points in both panels of Figure 22 are colored by redshift, and this shows that the

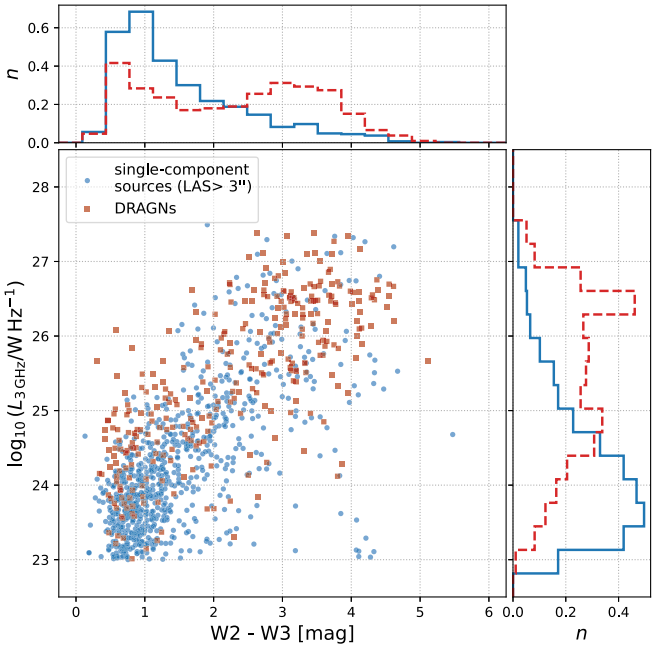

Figure 23. Comparison of the $W2 - W3$ colors and radio luminosities of DRAGNs (red) and extended (LAS > 3″) single-component radio sources (blue) where $W1 - W2 < 0.5$. Area normalized histograms of the two distributions are shown along the *x*- and *y*-axes using the same color scheme as the scatter plot.

passive/elliptical host galaxies are typically at lower redshift than the star-forming and (U)LIRG hosts. Recall that in Section 5.1 we showed that our single-component sources are typically less luminous than our DRAGNs. It is therefore prudent to check if the excess of passive/elliptical hosts for the single-component sources is simply the effect of better sampling the low-luminosity population of this sample. We compare the $W2 - W3$ colors and 3 GHz luminosities for DRAGNs and single-component radio sources that have host-dominated IR colors ($W1 - W2 < 0.5$) in Figure 23.

It is clear from Figure 23 that the different luminosity distributions of the two radio source samples are the dominant cause of the WISE color differences we observe. Qualitatively, at $L_{3\,\mathrm{GHz}} \gtrsim 10^{25}$ the single-component sources appear to have a similar $W2 - W3$ distribution to the DRAGNs. To test this in a more quantified manner, for each of our DRAGNs, we randomly select a single-component source controlling for both redshift and luminosity. This is achieved by requiring $\Delta L_{3\,\mathrm{GHZ}} < 0.2$ dex and $\Delta z < 0.01$, where $\Delta L_{3\,\mathrm{GHZ}}$ and Δz are the difference in radio luminosity and redshift, respectively, between a DRAGN and a randomly selected single-component source. We then perform a two-sample Kolmogorov–Smirnov test on the resultant $W2 - W3$, distributions, which returns a *p*-value of ≈0.3. Thus, when accounting for luminosity and redshift differences in the DRAGNs and single-component radio sources, we find no statistically significant differences in the $W2 - W3$ color distributions of DRAGNs and single-component radio sources.

The shift to bluer WISE colors with increasing radio luminosity is likely linked to accretion modes of the AGN. Radiatively efficient AGNs are more often found in galaxies with relatively young stellar populations than radiatively inefficient AGNs (e.g., Best & Heckman 2012; Janssen et al. 2012; Butler et al. 2018; Williams et al. 2018; Kondapally et al. 2022). At low radio luminosities, radiatively efficient AGNs

Table 3
Results of the Visual Inspection of Triple Sources Identified by DRAGNhunter

Name (1)	ArtFlag (2)
J000105.36−165940.3	1
J000108.78−123309.6	0
J000324.49+534446.2	0
J000402.24+332009.7	0
J000511.26−075558.4	0

Note. Columns: (1) name of the triple source, and (2) flag set 1 if visual inspection shows the triple to be a spurious detection.

(This table is available in its entirety in machine-readable form.)

only constitute a few percent of RLAGNs. However, at higher luminosities, the fraction of AGNs that are radiatively efficient increases, and accounts for approximately half of the RLAGN population at $L_{1.4\,\mathrm{GHz}} \sim 10^{25.5}\,\mathrm{W\,Hz^{-1}}$ (Best & Heckman 2012). Moreover, Mingo et al. (2022) showed in their Figure 5 that radiatively efficient AGNs in their data have blue W2 − W3 colors. Although we have made no effort to identify our AGNs as either radiatively efficient or inefficient in this work, it seems likely that the blue WISE colors of our DRAGNs may be an indicator of their accretion mode.

6. Triple Source Statistics

A third component is present in just over 10% of the DRAGNs (1836 objects). The additional component in these associations provides an opportunity for further analysis, for a couple of key reasons. First, the presence of a radio core is a robust indicator of the location of the AGN central engine, particularly for those sources without a host ID. Second, the relatively small number of triple sources means that a post hoc visual inspection of the triples to remove spurious detections is practical.

Each of these three-component sources is inspected by eye to identify contaminants that are not in fact DRAGNs, and 245 spurious detections are found. These are available in a machine-readable version of Table 3 (the first five rows are shown here to demonstrate its form and content), to aid scientists who wish to create reliable samples of triples from the VLASS Epoch 1 *Quick Look* catalog. However, we do not perform the visual inspection prior to the automated pipeline used to identify host IDs in order to maintain compatibility with future versions of the catalog (e.g., from subsequent VLASS epochs). In the remainder of this section we present statistics on the basic radio geometry and symmetry of these triple sources.

6.1. Flux Ratios and Arm Lengths of Radio Lobes

From their location on the *P–D* diagram (Figure 21), our DRAGNs are likely dominated by FR II morphologies. This is supported by the number of FR IIs seen when assessing the reliability of our catalog (e.g., see Figure 9). All things being equal, the lobes of FR IIs should have similar brightnesses. One key factor that might conflate this from the observer's point of view, is that of relativistic beaming. In this event, one would expect the brighter lobe to appear closer to the central AGN than the fainter lobe as a result of increased hotspot prominence (Magliocchetti et al. 1998; Harwood et al. 2020).

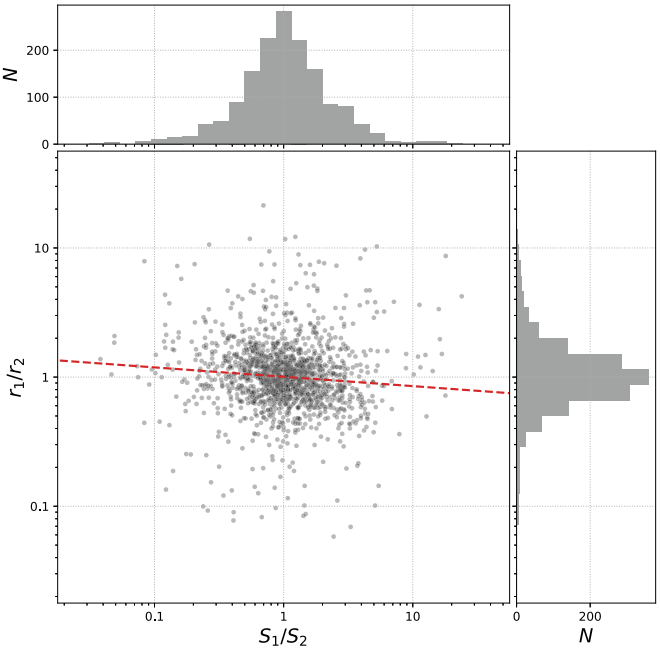

Figure 24. The lobe flux density ratio vs. arm length ratio for triple radio sources. Only the 1383 with relative errors of $< 10\%$ in both S_1/S_2 and r_1/r_2 are included. The red dashed line highlights the weak correlation between flux and geometric symmetry of the lobes of DRAGNs.

Table 4
Key Statistics for Lobe Flux and Arm Length Ratios in DRAGNs with a Host ID Coincident with a Radio Core

Statistic	Value
Spearman rank coefficient (ρ)	−0.12
p-value	4×10^{-6}
Flux ratio 68% spread	$1/2.2 < S_1/S_2 < 2.2$
Flux ratio 95% spread	$1/4.9 < S_1/S_2 < 4.9$
Arm length ratio 68% spread	$1/1.9 < r_1/r_2 < 1.9$
Arm length ratio 95% spread	$1/3.6 < r_1/r_2 < 3.6$

Each DRAGN has an "arm length" r_i from its core to each of its lobes, i, that have a flux density, S_i. Of our DRAGNs with cores, 1522 have a relative error in both arm length ratio, r_1/r_2, and lobe flux ratio, S_1/S_2, of $< 10\%$. For these sources, we list key statistics for the distributions S_1/S_2 and r_1/r_2 in Table 4, and plot these variables against each other in Figure 24. In our sample, we find a weak but significant correlation between S_1/S_2 and r_1/r_2, with a Spearman rank correlation coefficient of $\rho = -0.12$ and p-value of 4×10^{-6}. We highlight this correlation in Figure 24 with a red dashed line showing a least-squares fit to the data with a slope of -0.07 ± 0.02. This correlation shows a weak trend for the brighter component to be closer to the radio core than the fainter component, consistent with the findings of de la Rosa Valdés & Andernach (2019). The median LAS of this sample is 33″, and we split our sample into two subsets of small (LAS < 33″) and large (LAS ⩾ 33″) DRAGNs. Here we find that the correlation holds for large DRAGNs ($\rho = -0.18$, $p = 4 \times 10^{-7}$), but is not found for small DRAGNs ($\rho = -0.04$, $p = 0.24$). This likely results from the larger relative uncertainties in arm length measurements for smaller sources.

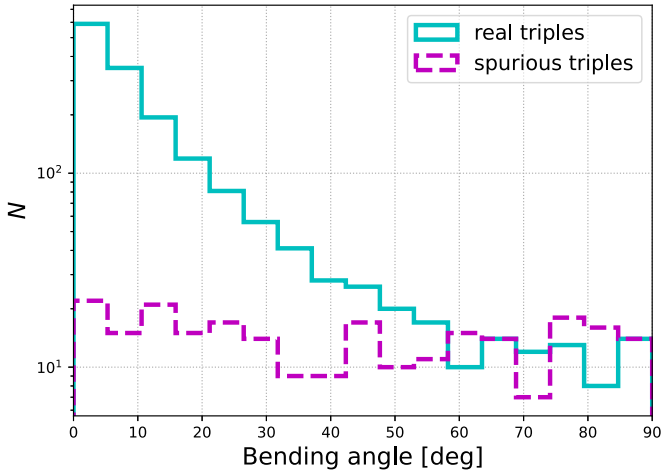

Figure 25. Distribution of bending angle measurements for triple sources. Real triple sources are shown by the cyan solid line, with the measurements for spurious triples shown by the magenta dashed line.

6.2. Jet Bending Angles in Triple Sources

The bending angle of a DRAGN is a measure of its deviation from a perfectly straight geometry. Using the component positions, we measure the bending angles of our triples, which range from 0° to 90°. A great majority have small bending angles, indicating that most three-component DRAGNs are straight or modestly bent. The fraction of contaminants depends heavily upon bending angle, dominating the catalog entries at high bending angles but reaching only a few percent at small bending angles (see Figure 25). This trend can be understood by noting that heavily bent real radio sources are relatively rare, while associations of artifacts in the VLASS quick look images often are distributed over a wide range in azimuth around bright sources.

In this section we have presented statistics on the flux and arm length symmetry, and jet bending angles of the triple sources identified by DRAGNHUNTER. In doing so we have taken no account of the host galaxy environment—an important factor that can impact all of these variables (Hardcastle & Krause 2013, 2014; Garon et al. 2019). For instance, Rodman et al. (2019) found that shorter lobe extents are found in denser environments based on a small sample of 16 FR IIs. The observations of Rodman et al. (2019) are supported by Yates-Jones et al. (2021) who, using numerical simulations, additionally found that dense environments are expected to produce brighter lobes. A number of studies have shown that bent-jet radio sources are more likely in dense environments with cluster winds acting to distort the morphology of the radio source (e.g., Blanton et al. 2000; Garon et al. 2019; Moravec et al. 2020; Morris et al. 2022). A follow-up to this work will analyze the relationship between galaxy environment and the bending angle of DRAGNs in VLASS (K. Achong et al. 2023, in preparation). While accounting for the host galaxy environment is beyond the scope of this work, the statistics that we report here are likely an interesting representation of the *global* population of DRAGNs.

7. Summary and Future Work

We have defined an algorithm, DRAGNHUNTER, to search for double-lobed radio sources using only survey component catalogs, and used this to construct a catalog of >17,000 DRAGNs in VLASS. This catalog has a reliability of ≈89%, rising to 93.5% if a host galaxy is identified, and >97% if selecting those DRAGNs with S/N in their angular size measurement >20 and a flux density ratio between the two lobes of <10. Although it is difficult to estimate the completeness of our sample without a "ground truth" catalog of DRAGNs in VLASS, comparisons with FIRST suggest that we identify ≳45% of DRAGNs with $S_{3\,\mathrm{GHZ}} > 20$ mJy and ≳85% at $S_{3\,\mathrm{GHZ}} > 100$ mJy. In addition to identifying the DRAGNs, we have used the likelihood ratio method to identify the probable hosts of more than 70% of our DRAGNs. Complementary to this, we identify hosts for more than 230,000 single-component radio sources. The catalog of these data will be made publicly available following publication of this paper via the Canadian Initiative for Radio Astronomy Data Analysis (CIRADA),[14] the CDS VizieR service[15](Ochsenbein et al. 2000), and as machine-readable tables (see the Appendix).

The DRAGNs cataloged in this work have properties consistent with being a larger, more powerful extension of the single-component radio galaxy population. On the radio *P–D* diagram, our DRAGNs reside in the region traditionally occupied by FR IIs. Although no additional morphological classification is attempted in this work, visual inspection of a random sample of these DRAGNs is also suggestive that our catalog consists predominantly of FR IIs. Exploring the extreme linear size regime of our catalog, we identify 31 previously undiscovered GRGs. The IR colors of the host galaxies of our DRAGNs are found to be consistent with the hosts of single-component sources when accounting for luminosity and redshift.

The VLASS *Quick Look* images used in this work are a rapidly produced data product and are known to have quality limitations. To enable rapid production, these images are only subject to shallow cleaning, and are not self-calibrated (Lacy et al. 2019). Consequently, while components are detected down to $S_{\mathrm{peak}} \approx 1$ mJy beam^{-1} in the *Quick Look* images, components fainter than $S_{\mathrm{peak}} \approx 3$ mJy beam^{-1} can suffer from unreliable measurements and a higher-than-expected contamination from spurious detections (Gordon et al. 2021). In the future, *Single Epoch* images that are less affected by these limitations will be available for the entire VLASS footprint (Lacy et al. 2022). For each epoch, this will allow catalogs of DRAGNs in VLASS to be produced using components with $S_{\mathrm{peak}} \gtrsim 600\,\mu$Jy beam^{-1}, and a three-epoch stack should allow for components down to $S_{\mathrm{peak}} \gtrsim 350\,\mu$Jy beam^{-1} to be used (Lacy et al. 2020). In addition to the added usable depth, the *Single Epoch* images will also provide spectral index information derived from the coefficients of the image Taylor-terms. These spectral indices can be used in determining whether a component is likely to be a lobe or a core, and may be useful in improving the reliability of the cataloged DRAGNs.

It is our hope that this catalog as is will prove a useful resource for the astronomical community. For instance, the large size and high reliability of this catalog make it a potential training set for machine-learning algorithms designed to identify DRAGNs. However, as with all work, there is room for improvement. Currently DRAGNs are selected by frequentist cuts to the input data. Thus, a clear direction for improving DRAGNHUNTER is to take a Bayesian approach to identifying DRAGNs. For example,

[14] www.cirada.ca
[15] https://vizier.cds.unistra.fr/index.gml

where a component is associated with multiple component pairs, rather than just taking the closest pairing, a probability of being the correct association can be assigned to each pair based various parameters such as the ratio of component flux densities or the presence of a host galaxy candidate between the components. This Bayesian philosophy will be the long-term focus for making DRAGNHUNTER as useful as possible for the coming generation of radio continuum surveys.

Acknowledgments

The authors thank the anonymous referee for providing a helpful report. Y.A.G. is supported by US National Science Foundation (NSF) grant AST 20-09441. Partial support for L. R. comes from US NSF grant AST 17-14205 to the University of Minnesota. H.A. benefited from grants CIIC 90/2020, 174/2021, and 138/2022 of Universidad de Guanajuato. L.K.M. was supported by the Medical Research Council [MR/T042842/1]. C.P.O., S.A.B., and A.N.V. are supported by NSERC, the Natural Sciences and Engineering Research Council of Canada. K.A. and C.B. acknowledge support from the NSF under Cooperative Agreement Nos. 1647375 and 1647378, including the Radio Astronomy Data Imaging and Analysis Lab (RADIAL) Research & Training Experience program. K.A. and C.B. further acknowledge support from the Alfred P. Sloan Foundation's Creating Equitable Pathways to STEM Graduate Education program and NSF grant AST 21-50222. The Canadian Initiative for Radio Astronomy Data Analysis (CIRADA) is funded by a grant from the Canada Foundation for Innovation 2017 Innovation Fund (Project 35999) and by the Provinces of Ontario, British Columbia, Alberta, Manitoba, and Quebec, in collaboration with the National Research Council of Canada, the US National Radio Astronomy Observatory and Australia's Commonwealth Scientific and Industrial Research Organisation.

The VLA is operated by NRAO, a facility of the National Science Foundation operated under cooperative agreement by Associated Universities, Inc.

WISE is a joint project of the University of California, Los Angeles, and the Jet Propulsion Laboratory/California Institute of Technology, and NEOWISE, which is a project of the Jet Propulsion Laboratory/California Institute of Technology. WISE and NEOWISE are funded by the National Aeronautics and Space Administration.

Funding for the SDSS IV has been provided by the Alfred P. Sloan Foundation, the U.S. Department of Energy Office of Science, and the Participating Institutions. SDSS acknowledges support and resources from the Center for High-Performance Computing at the University of Utah. The SDSS website is www.sdss.org. SDSS is managed by the Astrophysical Research Consortium for the Participating Institutions of the SDSS Collaboration including the Brazilian Participation Group, the Carnegie Institution for Science, Carnegie Mellon University, Center for Astrophysics, Harvard & Smithsonian (CfA), the Chilean Participation Group, the French Participation Group, Instituto de Astrofísica de Canarias, The Johns Hopkins University, Kavli Institute for the Physics and Mathematics of the Universe (IPMU)/University of Tokyo, the Korean Participation Group, Lawrence Berkeley National Laboratory, Leibniz Institut für Astrophysik Potsdam (AIP), Max-Planck-Institut für Astronomie (MPIA Heidelberg), Max-Planck-Institut für Astrophysik (MPA Garching), Max-Planck-Institut für Extraterrestrische Physik (MPE), National Astronomical Observatories of China, New Mexico State University, New York University, University of Notre Dame, Observatório Nacional/MCTI, The Ohio State University, Pennsylvania State University, Shanghai Astronomical Observatory, United Kingdom Participation Group, Universidad Nacional Autónoma de México, University of Arizona, University of Colorado Boulder, University of Oxford, University of Portsmouth, University of Utah, University of Virginia, University of Washington, University of Wisconsin, Vanderbilt University, and Yale University.

2MASS is a joint project of the University of Massachusetts and the Infrared Processing and Analysis Center/California Institute of Technology, funded by the National Aeronautics and Space Administration and the National Science Foundation.

The Legacy Surveys consist of three individual and complementary projects: the Dark Energy Camera Legacy Survey (DECaLS; Proposal ID No. 2014B-0404; PIs: David Schlegel and Arjun Dey), the Beijing-Arizona Sky Survey (BASS; NOAO Prop. ID No. 2015A-0801; PIs: Zhou Xu and Xiaohui Fan), and the Mayall z-band Legacy Survey (MzLS; Prop. ID No. 2016A-0453; PI: Arjun Dey). DECaLS, BASS, and MzLS together include data obtained, respectively, at the Blanco telescope, Cerro Tololo Inter-American Observatory, NSF's NOIRLab; the Bok telescope, Steward Observatory, University of Arizona; and the Mayall telescope, Kitt Peak National Observatory, NOIRLab. Pipeline processing and analyses of the data were supported by NOIRLab and the Lawrence Berkeley National Laboratory (LBNL). The Legacy Surveys project is honored to be permitted to conduct astronomical research on Iolkam Du'ag (Kitt Peak), a mountain with particular significance to the Tohono O'odham Nation.

NOIRLab is operated by the Association of Universities for Research in Astronomy (AURA) under a cooperative agreement with the National Science Foundation. LBNL is managed by the Regents of the University of California under contract to the U.S. Department of Energy.

This project used data obtained with the Dark Energy Camera (DECam), which was constructed by the Dark Energy Survey (DES) collaboration. Funding for the DES Projects has been provided by the U.S. Department of Energy, the U.S. National Science Foundation, the Ministry of Science and Education of Spain, the Science and Technology Facilities Council of the United Kingdom, the Higher Education Funding Council for England, the National Center for Supercomputing Applications at the University of Illinois at Urbana-Champaign, the Kavli Institute of Cosmological Physics at the University of Chicago, Center for Cosmology and Astro-Particle Physics at the Ohio State University, the Mitchell Institute for Fundamental Physics and Astronomy at Texas A&M University, Financiadora de Estudos e Projetos, Fundacao Carlos Chagas Filho de Amparo, Financiadora de Estudos e Projetos, Fundacao Carlos Chagas Filho de Amparo a Pesquisa do Estado do Rio de Janeiro, Conselho Nacional de Desenvolvimento Cientifico e Tecnologico and the Ministerio da Ciencia, Tecnologia e Inovacao, the Deutsche Forschungsgemeinschaft and the Collaborating Institutions in the Dark Energy Survey. The Collaborating Institutions are Argonne National Laboratory, the University of California at Santa Cruz, the University of Cambridge, Centro de Investigaciones Energeticas, Medioambientales y Tecnologicas-Madrid, the University of

Chicago, University College London, the DES-Brazil Consortium, the University of Edinburgh, the Eidgenossische Technische Hochschule (ETH) Zurich, Fermi National Accelerator Laboratory, the University of Illinois at Urbana-Champaign, the Institut de Ciencies de l'Espai (IEEC/CSIC), the Institut de Fisica d'Altes Energies, Lawrence Berkeley National Laboratory, the Ludwig Maximilians Universitat Munchen and the associated Excellence Cluster Universe, the University of Michigan, NSF's NOIRLab, the University of Nottingham, the Ohio State University, the University of Pennsylvania, the University of Portsmouth, SLAC National Accelerator Laboratory, Stanford University, the University of Sussex, and Texas A&M University.

BASS is a key project of the Telescope Access Program (TAP), which has been funded by the National Astronomical Observatories of China, the Chinese Academy of Sciences (the Strategic Priority Research Program "The Emergence of Cosmological Structures" grant No. XDB09000000), and the Special Fund for Astronomy from the Ministry of Finance. The BASS is also supported by the External Cooperation Program of Chinese Academy of Sciences (grant No. 114A11KYSB20160057), and Chinese National Natural Science Foundation (grant Nos. 12120101003 and 11433005).

The Legacy Survey team makes use of data products from the Near-Earth Object Wide-field Infrared Survey Explorer (NEOWISE), which is a project of the Jet Propulsion Laboratory/California Institute of Technology. NEOWISE is funded by the National Aeronautics and Space Administration.

The Legacy Surveys imaging of the DESI footprint is supported by the Director, Office of Science, Office of High Energy Physics of the U.S. Department of Energy under contract No. DE-AC02-05CH1123, by the National Energy Research Scientific Computing Center, a DOE Office of Science User Facility under the same contract; and by the U.S. National Science Foundation, Division of Astronomical Sciences under contract No. AST-0950945 to NOAO.

This work made use of the crossmatch service (Boch et al. 2012; Pineau et al. 2020) and the VizieR catalog access tool (Ochsenbein et al. 2000) provided by CDS, Strasbourg, France. It additionally used the facilities of the Canadian Astronomy Data Centre (CADC), an organization operated by the National Research Council of Canada with the support of the Canadian Space Agency. Observations from the VLA, WISE, SDSS, 2dFGRS, 6dFGS, 2MASS, and LS DR8 were used in this work.

Facilities: CDS, VLA, WISE, Sloan, CTIO:2MASS.

Software: The work carried out in this paper made use of the following software packages and tools: APLpy (Robitaille & Bressert 2012), AstroPy (Astropy Collaboration et al. 2013, 2018, 2022), Astroquery (Ginsburg et al. 2019), Matplotlib (Hunter 2007), NumPy (Harris et al. 2020), Pandas (McKinney 2010; pandas development team 2020), SAOImage DS9 (Joye & Mandel 2003), SciPy (Virtanen et al. 2020), Seaborn (Waskom 2021), and TOPCAT (Taylor 2005).

Appendix
Catalog Data Model

The catalog described within this paper will be released as two separated tables: (i) `Source and Host information`, and (ii) `DRAGN properties`. The `Source and host information` table lists main properties of all sources identified (single component and DRAGNs) as well as information on the AllWISE host and its redshift where available. The two catalog tables share a number of columns beyond what is necessary to enable table joining so as to maximize the standalone utility of each table. Tables 5 and 6 give the column descriptions for the `Source and Host information` and `DRAGN properties` tables, respectively. The full data tables are available in the online version of this article, as well as via CIRADA and the CDS VizieR service. Future versions of this catalog (e.g., using data from later VLASS epochs and *Single Epoch* images) will be released by CIRADA.

Table 5
Source and Host Information Table Column Descriptions

Column Number	Label	Description	Units
1	Name[a]	Name of the source	
2	RAdeg	R.A. of the source	deg
3	DEdeg	Decl. of the source	deg
4	Flux[b]	Total flux density of the source	mJy
5	e_Flux	Uncertainty in *Flux*	mJy
6	LAS	Estimate of the LAS of the source	arcseconds
7	e_LAS	Uncertainty in *LAS*	arcseconds
8	Type[c]	Type of source	
9	SourceFlag[d]	Source quality flag	
10	AllWISE	Name of the AllWISE host ID	
11	RAdegAllWISE	R.A. of the AllWISE host	deg
12	DEdegAllWISE	Decl. of the AllWISE host	deg
13	SepAllWISE	Angular separation between radio source and AllWISE host ID	arcseconds
14	LR	Likelihood ratio of host ID	
15	Rel	Probabilty that the host is correct	
16	HostFlag[e]	Host ID flag	
17	W1mag	Vega magnitude of AllWISE host in the W1 band	mag
18	e_W1mag	Uncertainty in *W1mag*	mag
19	W2mag	Vega magnitude of AllWISE host in the W1 band	mag
20	e_W2mag	Uncertainty in *W2mag*	mag
21	W3mag	Vega magnitude of AllWISE host in the W1 band	mag
22	e_W3mag	Uncertainty in *W3mag*	mag
23	W4mag	Vega magnitude of AllWISE host in the W1 band	mag
24	e_W4mag	Uncertainty in *W4mag*	mag
25	z	Host redshift	
26	e_z	Uncertainty in z	
27	f_z	Redshift type	
28	r_z	Survey that the redshift was obtained from	

Notes. This table contains 595,375 rows and is provided in a machine-readable format.
[a] For single-component sources, this is the Julian *Component_name* from the VLASS Quick Look component catalog (Gordon et al. 2021) to allow for easy joining with that catalog. For DRAGNs, the *Name* is a Julian name of the format Jhhmmss.ss ± ddmmss.s.
[b] This is the sum of the cataloged fluxes of all associated components. The flux-scaling correction of $1/0.87$ recommended in Gordon et al. (2021) has not been applied to these values and is left to the discretion of the end-user.
[c] "S" is a single-component source; "D" is a DRAGN.
[d] Set to 1 if Type = "D" and either Lobe_flux_ratio < 0.1 or Lobe_flux_ratio > 10 or LAS/E_LAS < 20. For all other sources, this flag is set to 0.
[e] Set to -2 if the LR identified host of a DRAGN is colocated with a radio core, -1 if the LR identified host of a DRAGN has been replaced by a host candidate coincident with a core, 0 for single-component sources and DRAGNs without a radio core, and 1 for DRAGNs with a radio core that is not colocated with a host candidate.

(This table is available in its entirety in machine-readable form.)

Table 6
DRAGN Properties Table Column Descriptions

Column Number	Label	Description	Units
1	Name	Julian name of the source	
2	RAdeg	R.A. of the source	deg
3	DEdeg	Decl. of the source	deg
4	Flux[b]	Total flux density of the source	mJy
5	e_Flux	Uncertainty in *Flux*	mJy
6	CoreProm	Fraction of *Flux* associated with *Core*	
7	e_CoreProm	Uncertainty in *CoreProm*	
8	LobeFluxRatio	Ratio of the flux from *Lobe1* to the flux from *Lobe2*	
9	e_LobeFluxRatio	Uncertainty in *LobeFluxRatio*	
10	LAS	Estimate of the LAS of the source	arcseconds
11	e_LAS	Uncertainty in *LAS*	arcseconds
12	Misalign1[f]	Relative misalignment of *Lobe1*	deg
13	e_Misalign1	Uncertainty in *Misalign1*	deg
14	Misalign2[f]	Relative misalignment of *Lobe2*	deg
15	e_Misalign2	Uncertainty in *Misalign2*	deg
16	MeanMisalign	Mean value of *Misalign1* and *Misalign2*	deg

Table 6
(Continued)

Column Number	Label	Description	Units
17	e_MeanMisalign	Uncertainty in *MeanMisalign*	deg
18	Lobe1	Component name of *Lobe1*	
19	Lobe2	Component name of *Lobe2*	
20	Core	Component name of *Core* if identified	
21	RAdegCore	R.A. of *Core*	deg
22	DEdegCore	Decl. of *Core*	deg
23	RAdegMedian	Median R.A. of two lobes	deg
24	DEdegMedian	Median Decl. of two lobes	deg
25	RAdegFW	Flux-weighted central R.A. of two lobes	deg
26	DEdegFW	Flux-weighted central Decl. of two lobes	deg
27	SourceFlag[d]	Source quality flag	
28	AllWISE	Name of the AllWISE host ID	
29	SepAllWISE	Angular separation between radio source and AllWISE host ID	arcseconds
30	LR	Likelihood ratio of host ID	
31	Rel	Probabilty that the host is correct	
32	HostFlag[e]	Host ID flag	

Notes. This table contains 17,724 rows and is provided in a machine-readable format.
[b] This is the sum of the cataloged fluxes of all associated components. The flux-scaling correction of 1/0.87 recommended in Gordon et al. (2021) has not been applied to these values and is left at the discretion of the end-user.
[d] Set to 1 if either Lobe_flux_ratio < 0.1 or Lobe_flux_ratio > 10 or LAS/E_LAS < 20. For all other sources, this flag is set to 0.
[e] Set to -2 if the LR identified host of a DRAGN is colocated with a radio core, -1 if the LR identified host of a DRAGN has been replaced by a host candidate coincident with a core, 0 for single-component sources and DRAGNs without a radio core, and 1 for DRAGNs with a radio core that is not colocated with a host candidate.
[f] Components with low aspect ratios (nearly circular geometry) can have large uncertainties in their measured misalignments. Users are advised to make use of the appropriate uncertainty measurements provided (E_Misalign_n) if using these values.

(This table is available in its entirety in machine-readable form.)

ORCID iDs

Yjan A. Gordon https://orcid.org/0000-0003-1432-253X
Lawrence Rudnick https://orcid.org/0000-0001-5636-7213
Heinz Andernach https://orcid.org/0000-0003-4873-1681
Leah K. Morabito https://orcid.org/0000-0003-0487-6651
Christopher P. O'Dea https://orcid.org/0000-0001-6421-054X
Kaylan-Marie Achong https://orcid.org/0000-0002-7726-2792
Stefi A. Baum https://orcid.org/0000-0002-4735-8224
Eric J. Hooper https://orcid.org/0000-0003-0713-3300
Beatriz Mingo https://orcid.org/0000-0001-5649-938X
Melissa E. Morris https://orcid.org/0000-0001-9920-0210
Adrian N. Vantyghem https://orcid.org/0000-0003-4227-4838

References

Ahumada, R., Prieto, C. A., Almeida, A., et al. 2020, ApJS, 249, 3
Alexander, P. 2000, MNRAS, 319, 8
An, T., & Baan, W. A. 2012, ApJ, 760, 77
Andernach, H., Jiménez-Andrade, E. F., & Willis, A. G. 2021, Galax, 9, 99
Assef, R. J., Stern, D., Kochanek, C. S., et al. 2013, ApJ, 772, 26
Astropy Collaboration, Price-Whelan, A. M., Lim, P. L., et al. 2022, ApJ, 935, 167
Astropy Collaboration, Price-Whelan, A. M., Sipőcz, B. M., et al. 2018, AJ, 156, 123
Astropy Collaboration, Robitaille, T. P., Tollerud, E. J., et al. 2013, A&A, 558, A33
Baldry, I. K., Liske, J., Brown, M. J. I., et al. 2018, MNRAS, 474, 3875
Baldwin, J. E. 1982, in IAU Symp. 97, Extragalactic Radio Sources, ed. D. S. Heeschen & C. M. Wade (Dordrecht: D. Reidel), 21
Banfield, J. K., Wong, O. I., Willett, K. W., et al. 2015, MNRAS, 453, 2326
Beck, R., Dobos, L., Budavári, T., Szalay, A. S., & Csabai, I. 2016, MNRAS, 460, 1371
Beck, R., Szapudi, I., Flewelling, H., et al. 2021, MNRAS, 500, 1633
Becker, R. H., Helfand, D. J., White, R. L., Gregg, M. D., & Laurent-Muehleisen, S. A. 2003, yCat, VIII/71
Becker, R. H., White, R. L., & Helfand, D. J. 1995, ApJ, 450, 559
Begelman, M. C., & Cioffi, D. F. 1989, ApJL, 345, L21
Bell, E. F. 2003, ApJ, 586, 794
Best, P. N., & Heckman, T. M. 2012, MNRAS, 421, 1569
Best, P. N., Kauffmann, G., Heckman, T. M., & Ivezić, Ž. 2005, MNRAS, 362, 9
Bicknell, G. V. 1985, PASA, 6, 130
Blake, C., & Wall, J. 2002, MNRAS, 337, 993
Blandford, R., Meier, D., & Readhead, A. 2019, ARA&A, 57, 467
Blandford, R. D., & Rees, M. J. 1974, MNRAS, 169, 395
Blanton, E. L., Gregg, M. D., Helfand, D. J., Becker, R. H., & White, R. L. 2000, ApJ, 531, 118
Blanton, M. R., Bershady, M. A., Abolfathi, B., et al. 2017, AJ, 154, 28
Blundell, K. M., Rawlings, S., & Willott, C. J. 1999, AJ, 117, 677
Boch, T., Pineau, F., & Derriere, S. 2012, in ASP Conf. Ser. 461, Astronomical Data Analysis Software and Systems XXI, ed. P. Ballester, D. Egret, & N. P. F. Lorente (San Francisco, CA: ASP), 291
Bovy, J., Hennawi, J. F., Hogg, D. W., et al. 2011, ApJ, 729, 141
Bridle, A. H. 1984, AJ, 89, 979
Bridle, A. H., Davis, M. M., Meloy, D. A., et al. 1976, Natur, 262, 179
Butler, A., Huynh, M., Delvecchio, I., et al. 2018, A&A, 620, A16
Cameron, E. 2011, PASA, 28, 128
Chambers, K. C., Magnier, E. A., Metcalfe, N., et al. 2016, arXiv:1612.05560
Ching, J. H. Y., Sadler, E. M., Croom, S. M., et al. 2017, MNRAS, 464, 1306
Colless, M., Dalton, G., Maddox, S., et al. 2001, MNRAS, 328, 1039
Condon, J. J., Cotton, W. D., Greisen, E. W., et al. 1998, AJ, 115, 1693
Cotter, G., Rawlings, S., & Saunders, R. 1996, MNRAS, 281, 1081
Cress, C. M., Helfand, D. J., Becker, R. H., Gregg, M. D., & White, R. L. 1996, ApJ, 473, 7
Croton, D. J. 2006, MNRAS, 369, 1808
Cutri, R. M., et al. 2012, yCat, II/311
Cutri, R. M., Wright, E. L., Conrow, T., et al. 2013, Explanatory Supplement to the AllWISE Data Release Products

Dabhade, P., Gaikwad, M., Bagchi, J., et al. 2017, MNRAS, 469, 2886
Dabhade, P., Mahato, M., Bagchi, J., et al. 2020a, A&A, 642, A153
Dabhade, P., Röttgering, H. J. A., Bagchi, J., et al. 2020b, A&A, 635, A5
de la Rosa Valdés, P. A., & Andernach, H. 2019, arXiv:1908.09988
Dey, A., Schlegel, D. J., Lang, D., et al. 2019, AJ, 157, 168
Donley, J. L., Koekemoer, A. M., Brusa, M., et al. 2012, ApJ, 748, 142
Drinkwater, M. J., Byrne, Z. J., Blake, C., et al. 2018, MNRAS, 474, 4151
Drinkwater, M. J., Jurek, R. J., Blake, C., et al. 2010, MNRAS, 401, 1429
Driver, S. P., Hill, D. T., Kelvin, L. S., et al. 2011, MNRAS, 413, 971
Duncan, K. J. 2022, MNRAS, 512, 3662
Fanaroff, B. L., & Riley, J. M. 1974, MNRAS, 167, 31P
Ferrarese, L., & Merritt, D. 2000, ApJL, 539, L9
Fleuren, S., Sutherland, W., Dunne, L., et al. 2012, MNRAS, 423, 2407
Galvin, T. J., Huynh, M., Norris, R. P., et al. 2019, PASP, 131, 108009
Galvin, T. J., Huynh, M. T., Norris, R. P., et al. 2020, MNRAS, 497, 2730
Garon, A. F., Rudnick, L., Wong, O. I., et al. 2019, AJ, 157, 126
Garrington, S. T., Leahy, J. P., Conway, R. G., & Laing, R. A. 1988, Natur, 331, 147
Ginsburg, A., Sipőcz, B. M., Brasseur, C. E., et al. 2019, AJ, 157, 98
Gordon, Y. A., Boyce, M. M., O'Dea, C. P., et al. 2021, ApJS, 255, 30
Gürkan, G., Hardcastle, M. J., & Jarvis, M. J. 2014, MNRAS, 438, 1149
Gürkan, G., Prandoni, I., O'Brien, A., et al. 2022, MNRAS, 512, 6104
Hale, C. L., McConnell, D., Thomson, A. J. M., et al. 2021, PASA, 38, e058
Hardcastle, M. J., & Croston, J. H. 2020, NewAR, 88, 101539
Hardcastle, M. J., Gürkan, G., van Weeren, R. J., et al. 2016, MNRAS, 462, 1910
Hardcastle, M. J., & Krause, M. G. H. 2013, MNRAS, 430, 174
Hardcastle, M. J., & Krause, M. G. H. 2014, MNRAS, 443, 1482
Hardcastle, M. J., Williams, W. L., Best, P. N., et al. 2019, A&A, 622, A12
Harris, C. R., Millman, K. J., van der Walt, S. J., et al. 2020, Natur, 585, 357
Harrison, C. M. 2017, NatAs, 1, 0165
Harwood, J. J., Vernstrom, T., & Stroe, A. 2020, MNRAS, 491, 803
Heinz, S., Reynolds, C. S., & Begelman, M. C. 1998, ApJ, 501, 126
Hubbard, A., & Blackman, E. G. 2006, MNRAS, 371, 1717
Huchra, J. P., Macri, L. M., Masters, K. L., et al. 2012, ApJS, 199, 26
Hunter, J. D. 2007, CSE, 9, 90
Ishwara-Chandra, C. H., & Saikia, D. J. 1999, MNRAS, 309, 100
Janssen, R. M. J., Röttgering, H. J. A., Best, P. N., & Brinchmann, J. 2012, A&A, 541, A62
Jarvis, M. E., Harrison, C. M., Thomson, A. P., et al. 2019, MNRAS, 485, 2710
Jones, D. H., Saunders, W., Colless, M., et al. 2004, MNRAS, 355, 747
Jones, D. H., Saunders, W., Read, M., & Colless, M. 2005, PASA, 22, 277
Joye, W. A., & Mandel, E. 2003, in ASP Conf. Ser. 295, Astronomical Data Analysis Software and Systems XII, ed. H. E. Payne, R. I. Jedrzejewski, & R. N. Hook (San Francisco, CA: ASP), 489
Kondapally, R., Best, P. N., Cochrane, R. K., et al. 2022, MNRAS, 513, 3742
Kozieł-Wierzbowska, D., Goyal, A., & Żywucka, N. 2020, ApJS, 247, 53
Kuźmicz, A., & Jamrozy, M. 2021, ApJS, 253, 25
Kuźmicz, A., Jamrozy, M., Bronarska, K., Janda-Boczar, K., & Saikia, D. J. 2018, ApJS, 238, 9
Lacy, M., Baum, S. A., Chandler, C. J., et al. 2020, PASP, 132, 035001
Lacy, M., Meyers, S. T., Chandler, C., et al. 2019, VLASS Project Memo 13: Pilot and Epoch 1 Quick Look Data Release, https://library.nrao.edu/public/memos/vla/vlass/VLASS_013.pdf
Lacy, M., Patil, P., & Nyland, K. 2022, VLASS Project Memo 17: Characterization of VLASS Single Epoch Continuum Validation Products, https://library.nrao.edu/public/memos/vla/vlass/VLASS_017.pdf
Laing, R. A. 1988, Natur, 331, 149
Laing, R. A., & Bridle, A. H. 2014, MNRAS, 437, 3405
Lang, D. 2014, AJ, 147, 108
Leahy, J. P. 1993, in Jets in Extragalactic Radio Sources, ed. H.-J. Röser & K. Meisenheimer (Berlin: Springer), 1
Leahy, J. P., & Perley, R. A. 1995, MNRAS, 277, 1097
Magliocchetti, M., Maddox, S. J., Lahav, O., & Wall, J. V. 1998, MNRAS, 300, 257
McAlpine, K., Smith, D. J. B., Jarvis, M. J., Bonfield, D. G., & Fleuren, S. 2012, MNRAS, 423, 132
McKinney, W. 2010, in Proc. 9th Python in Science Conf., ed. S. van der Walt & J. Millman, 56
Miley, G. 1980, ARA&A, 18, 165
Mingo, B., Croston, J. H., Best, P. N., et al. 2022, MNRAS, 511, 3250
Mingo, B., Croston, J. H., Hardcastle, M. J., et al. 2019, MNRAS, 488, 2701
Mingo, B., Watson, M. G., Rosen, S. R., et al. 2016, MNRAS, 462, 2631
Moravec, E., Gonzalez, A. H., Dicker, S., et al. 2020, ApJ, 898, 145
Morganti, R., Oosterloo, T., Tadhunter, C., Bernhard, E. P., & Raymond Oonk, J. B. 2021, A&A, 656, A55
Morris, M. E., Wilcots, E., Hooper, E., & Heinz, S. 2022, AJ, 163, 280
Norman, M. L., Winkler, K. H. A., Smarr, L., & Smith, M. D. 1982, A&A, 113, 285
Norris, R. P. 2017, NatAs, 1, 671
Norris, R. P., Hopkins, A. M., Afonso, J., et al. 2011, PASA, 28, 215
Norris, R. P., Marvil, J., Collier, J. D., et al. 2021, PASA, 38, e046
Ochsenbein, F., Bauer, P., & Marcout, J. 2000, A&AS, 143, 23
O'Dea, C. P., & Baum, S. A. 1997, AJ, 113, 148
O'Dea, C. P., Koekemoer, A. M., Baum, S. A., et al. 2001, AJ, 121, 1915
O'Dea, C. P., & Saikia, D. J. 2021, A&ARv, 29, 3
Oei, M. S. S. L., van Weeren, R. J., Gast, A. R. D. J. G. I. B., et al. 2023, A&A, 672, A163
Oei, M. S. S. L., van Weeren, R. J., Hardcastle, M. J., et al. 2022, A&A, 660, A2
Padovani, P. 2017, NatAs, 1, 0194
pandas development team 2020, pandas-dev/pandas: Pandas, v1.4.1 Zenodo, doi:10.5281/zenodo.3509134
Pineau, F.-X., Boch, T., Derrière, S., & Schaaff, A. 2020, in ASP Conf. Ser. 522, Astronomical Data Analysis Software and Systems XXVII, ed. P. Ballester et al. (San Francisco, CA: ASP), 125
Proctor, D. D. 2011, ApJS, 194, 31
Reynolds, C. S., & Begelman, M. C. 1997, ApJL, 487, L135
Robitaille, T., & Bressert, E. 2012, APLpy: Astronomical Plotting Library in Python, Astrophysics Source Code Library, ascl:1208.017
Rodman, P. E., Turner, R. J., Shabala, S. S., et al. 2019, MNRAS, 482, 5625
Sadler, E. M., Cannon, R. D., Mauch, T., et al. 2007, MNRAS, 381, 211
Scaife, A. M. M., & Porter, F. 2021, MNRAS, 503, 2369
Schinnerer, E., Carilli, C. L., Scoville, N. Z., et al. 2004, AJ, 128, 1974
Schinnerer, E., Smolčić, V., Carilli, C. L., et al. 2007, ApJS, 172, 46
Schoenmakers, A. P., de Bruyn, A. G., Röttgering, H. J. A., & van der Laan, H. 2001, A&A, 374, 861
Shimwell, T. W., Hardcastle, M. J., Tasse, C., et al. 2022, A&A, 659, A1
Shimwell, T. W., Röttgering, H. J. A., Best, P. N., et al. 2017, A&A, 598, A104
Shimwell, T. W., Tasse, C., Hardcastle, M. J., et al. 2019, A&A, 622, A1
Skrutskie, M. F., Cutri, R. M., Stiening, R., et al. 2006, AJ, 131, 1163
Smolčić, V., Novak, M., Bondi, M., et al. 2017, A&A, 602, A1
Sutherland, R. S., & Bicknell, G. V. 2007, Ap&SS, 311, 293
Sutherland, W., & Saunders, W. 1992, MNRAS, 259, 413
Sweijen, F., van Weeren, R. J., Röttgering, H. J. A., et al. 2022, NatAs, 6, 350
Taylor, M. B. 2005, in ASP Conf. Ser. 347, Astronomical Data Analysis Software and Systems XIV, ed. P. Shopbell, M. Britton, & R. Ebert (San Francisco, CA: ASP), 29
Vardoulaki, E., Jiménez Andrade, E. F., Delvecchio, I., et al. 2021, A&A, 648, A102
Virtanen, P., Gommers, R., Oliphant, T. E., et al. 2020, NatMe, 17, 261
Waskom, M. L. 2021, JOSS, 6, 3021
White, R. L., Becker, R. H., Helfand, D. J., & Gregg, M. D. 1997, ApJ, 475, 479
Williams, W. L., Calistro Rivera, G., Best, P. N., et al. 2018, MNRAS, 475, 3429
Williams, W. L., Hardcastle, M. J., Best, P. N., et al. 2019, A&A, 622, A2
Willis, A. G., Strom, R. G., & Wilson, A. S. 1974, Natur, 250, 625
Wright, E. L., Eisenhardt, P. R. M., Mainzer, A. K., et al. 2010, AJ, 140, 1868
Wu, C., Wong, O. I., Rudnick, L., et al. 2019, MNRAS, 482, 1211
Yates-Jones, P. M., Shabala, S. S., & Krause, M. G. H. 2021, MNRAS, 508, 5239
York, D. G., Adelman, J., Anderson, J. E. J., et al. 2000, AJ, 120, 1579
Zhou, R., Newman, J. A., Mao, Y.-Y., et al. 2021, MNRAS, 501, 3309